Journal of
Marine Science and Engineering

MDPI

Article

Design and Testing of a Spherical Autonomous Underwater Vehicle for Shipwreck Interior Exploration

Ross Eldred *, Johnathan Lussier and Anthony Pollman

Systems Engineering Department, US Naval Postgraduate School, Monterey, CA 93943, USA; jonathan.lussier@du.edu (J.L.); agpollma@nps.edu (A.P.)
* Correspondence: ross.eldred@nps.edu; Tel.: +1-831-656-6941

Abstract: This article details the design, construction and implementation of a novel, spherical unmanned underwater vehicle (UUV) prototype for operations within confined, entanglement-prone marine environments. The nature of shipwreck interiors, the exploration of which the vehicle was originally designed, imposes special risks that constrain system requirements while promoting other attributes uncommon in typical open-water UUV designs. The invention, the Wreck Interior Exploration Vehicle (WIEVLE), was constructed using 3-D additive manufacturing technology combined with relatively inexpensive commercial components. Similar inventions are compared, followed by a thorough review of the physical and functional characteristics of the system. The key attributes of the design include a smooth, spherical hull with 360-degree sensor coverage, and a fixed, upward-angled thruster core, relying on inherent buoyancy to take the place of a dedicated depth-changing mechanism. Initial open-loop control testing demonstrated stable 4 degrees of freedom (DOF) maneuvering capability. The article concludes with an overview of the results of the initial testing, a review of how the key system design attributes address the unique shipwreck interior exploration challenges, and a plan for the future development of the platform.

Keywords: spherical underwater vehicle; AUV; hovering autonomous underwater vehicle; spherical hull; confined space inspection; shipwreck interior exploration; littoral operations; extreme environment exploration

Citation: Eldred, R.; Lussier, J.; Pollman, A. Design and Testing of a Spherical Autonomous Underwater Vehicle for Shipwreck Interior Exploration. *J. Mar. Sci. Eng.* **2021**, *9*, 320. https://doi.org/10.3390/jmse9030320

Academic Editors: Worakanok Thanyamanta and Mario Brito

Received: 29 January 2021
Accepted: 10 March 2021
Published: 14 March 2021

1. Introduction

1.1. Shipwreck Interior Exploration

Special risks and constraints plague the exploration of submerged, enclosed spaces like shipwrecks [1–3]. Such challenges include tight maneuvering space, obstructions and entanglement hazards, as well as poor visibility caused by the disturbance of fine sediment, which may be settled on wreck structure throughout the interior. The extraordinary risks associated with both manned and unmanned missions into these environments make smooth-hulled, tetherless autonomous underwater vehicles (AUVs) among the best technological solutions. This article describes the design and initial testing of the Wreck Interior Exploration Vehicle (WIEVLE)—a novel AUV prototype currently under development at the U.S. Naval Postgraduate School in Monterey, California—with emphasis on the design characteristics of its spherical hull and quad-core, angled propulsion system.

For centuries, humankind has desired to explore extreme environments. Shipwrecks, in particular, have long been attractive targets for the adventurous entrepreneur, leading some explorers to riches and glory, and others to their deaths. Often, the task of exploring a particular shipwreck does not require entering the wreck itself. In many cases, especially antiquated wrecks in a saltwater environment, the wreck has collapsed and there is no longer an "interior" to explore. Some objectives, however, can only be realized by venturing inside. This is shipwreck interior exploration (SIE). Few environments on earth are more hostile to both man and machine.

SIE mission capability may be very valuable to certain stakeholders, particularly within the defense, archaeology, salvage and emergency response sectors. The U.S. government, in one famous example, once attempted to covertly raise a Soviet nuclear submarine wreck in 1974, at enormous risk and expense [4]. A surface vessel, the *Glomar Explorer*, was disguised as a seabed mining platform and concealed a "moon pool" access bay and a unique, claw-like capturing mechanism, lowered by cable, for grasping and hoisting the wreck from a depth of over 5000 m up into its bay. The mission, one of the most expensive and elaborate espionage attempts in history, was a partial success; half of the submarine was recovered, with the other half breaking away during the recovery [4].

Sometimes critical information, such as the wreck's identity, can only be revealed by examining physical artifacts inside the shipwreck [5,6]. Underwater explorers John Chatterton and Richie Kohler entered the wreck of an un-identified World War II German U-boat multiple times in an effort to identify it [5]. Their goal was the retrieval of a metal equipment tag which they believed may be engraved with the U-boat's hull number. Although other divers perished in their efforts to beat them to the discovery, Chatterton and Kohler were ultimately successful in retrieving the placard that positively identified the wreck as U-869.

Occasionally, keen interest is placed on specific items within a shipwreck, and SIE is required to locate, surveille, or recover them. These items-of-interest may include treasure, artifacts, recently sunken property, environmental hazards, and even humans—living or deceased. One notable example, the K-278 *Komsomolets*, a then-state-of-the-art, double titanium-hulled, Soviet nuclear submarine, sank in 1984 after an uncontrolled fire, carrying with it two torpedoes with tactical nuclear warheads [7,8]. The hull of the torpedo-containing bow section suffered major damage subsequent to the sinking, after an explosion took place inside the wreck, leaving significant breaches in the hull. A Norwegian study [8] found that "neither the submarine hull nor the reactor vessel will be destroyed by corrosion for at least 1000 years." The application of SIE to address the security and environmental risks associated with this wreck are self-evident. Although SIE alternatives include both human divers and remote technology, only remote technology will be further considered in this work since most wrecks rest at depths greater than humans are currently capable of diving.

1.2. SIE in Historical Context—Traditional and Modern Approaches to Shipwreck Exploration and Survey

1.2.1. The Traditional Approach: The Remotely Operated Vehicle (ROV) Survey

Perhaps the most famous early example of a multi-system approach to SIE dates back to Dr. Robert Ballard's 1986 follow-up expedition to the recently discovered wreck of the RMS *Titanic*. On this particular manned mission, the pilots of the submersible *Alvin* flew the tethered ROV Jason Jr. into the well of *Titanic's* Grand Staircase, capturing some of the most stunning images of a shipwreck interior ever recorded [9]. The pilots had hoped to use Jason Jr. to penetrate the wreck at other locations as well, and although they displayed great skill and Jason Jr. performed admirably, the tight maneuvering space, sediment and the risk of entangling the tether were too great. As a result of the ROV's limitations, some likely spectacular images of Titanic's interior may be lost forever to the relentless, punishing decomposition of time and eternal darkness.

A more common, traditional approach to external surveys incorporates the use of the tow sled, usually equipped with a side scan sonar [10], or optical sensors, like the *Argus* tow sled, which was used in 2000 to survey over 50 archaeological sites in the Black Sea [11]. The production of high resolution photomosaics, which greatly aid marine archaeology, and the recovery of external artifacts, have been achieved through the use of sophisticated ROVs such as Hercules, which was used to retrieve artifacts from a deep-water archaeological site in the Black Sea in 2007 [12]. Although the use of a tow sled for external survey is well documented and has led to many successful discoveries, the cost of these traditional operations, which involve surface support vessels with dynamic positioning (DP) capability, ROV pilots and support crew, can be very high (over $40,000 per day), making the AUV

an attractive alternative [6,13]. Additionally, mini-ROVs like Nemo, which was used to explore the wreck of the *Costa Cordia* [14], have more recently become popular as they are less expensive than their larger cousins requiring DP-capable vessels.

1.2.2. The Modern Approach: Multi-System Autonomous Vehicle Survey

A significant reduction in risk and cost, when compared with traditional ROV exploration, has been achieved by combining the capabilities of autonomous vehicles to create accurate, geo-referenced surveys of shipwrecks. Rutledge et al. propose a five-step methodology for the use of AUVs to search for underwater historical sites [15]. These processes include (1) the scanning of the search area from a "high altitude" to collect side scan sonar imagery with relatively low resolution, (2) processing the imagery to identify potential targets, (3) ranking the resulting targets (an important step given limited vehicle endurance), (4) planning the AUV path, visiting targets in order of importance, and (5) deploying the AUV to execute the planned path at closer proximity to the wreck to obtain higher-resolution imagery [15]. Rutledge's methodology was successfully implemented off the coast of Malta to survey wreck sites using the relatively low-cost OceanServer IVER3 AUV [15,16].

The modern multi-system approach to exterior survey typically utilizes a combination of sensor technology, including single-beam and multi-beam echosounders (SBES and MBES, respectively), side scan sonar (SSS), and high-definition (HD) video. These sensors enable researchers to locate the site, create a geo-referenced bathymetric map of the wreck site on the bottom, and sometimes even create a 3-D photomosaic of the wreck itself, which may be processed for viewing in a virtual reality (VR) simulation [6]. The autonomous vehicles employed may include combinations of unmanned aerial vehicles (UAVs), autonomous surface vehicles (ASVs), and AUVs or ROVs. Kapetanović et al. used a multi-system approach to lake bottom bathymetric mapping [17], and cultural heritage sites [18], incorporating an ASV in conjunction with a UAV. A wreck site, discovered in 2007 by the Norwegian Hydrographic Service was later identified in 2015 as the Figaro, a whaling vessel which sank in 1908 [19], using a REMUS 100 AUV, equipped with SSS, in conjunction with a Seabotix LBV 200 ROV, equipped with an HD camera. The Archaeological Robot Systems for the Worlds Seas (ARROWS) project, undertaken from 2012–2015 with the objective of developing a low-cost method for underwater archaeology, resulted in another autonomous multi-system approach to site survey [2]. Three autonomous vehicles were developed as result of the ARROWS I effort; (1) the MARTA, a surface and sub-surface navigating, hovering AUV equipped with a sonar, (2) the A-Size AUV, and (3) the shipwreck-penetration capable U-CAT AUV (further discussed in Section 1.3) [2].

1.3. Prior Work in Confined-Space Underwater Vehicles

Although the freedom afforded by the typical, open-water operating environment is usually amenable to large (most commonly torpedo-shaped) AUVs, recently, several spherical, or spheroid, smooth-hulled UUVs have been developed. These vehicles benefit from greater maneuverability in tight spaces, as a sphere can occupy a constant volume of space as it executes a "zero-radius" turn. A smooth exterior further reduces entanglement risk. These vehicles range from the highly advanced sensor platforms exploring un-mapped caves or flooded mine systems to small experimental vehicles intended to prove new methods of propulsion and control. In each example described in this section, the common challenges of AUV design are amplified by the constraints of the extreme environments in which they were designed to explore. Most exhibit smooth, round exteriors with limited internal volume and a-typical propulsion methods. The target operating environments for these vehicles include chemical ponds, nuclear power plants, littorals, flooded mines and caves, and oil rig structures. The key difference between the shipwreck interior environment and these environments, however, is the combination of extremely restricted maneuvering space, entanglement hazards and settled sediment at all levels of the water column in which the AUV must navigate (in contrast, for example, with the floor of a

smooth-walled cave). The vehicles examined include a spherical ROV, conceptual and ultra-compact AUVs, larger, advanced/commercial AUVs, and the four vehicles most similar to WIEVLE. The SIE capability gaps are summarized at the end of each subsection.

1.3.1. Spherical ROV

The Eyeball ROV, developed at MIT ca. 2011, was designed for inspection tasks in hazardous environments [20]. Although not autonomous, this vehicle is mentioned here due to its novel spherical shape and gimballed control mechanism. The prototype incorporates a hull under 20 cm in diameter, with a pair of externally mounted thrusters for translation and yaw control, while pitch and roll are controlled via a gimballed, eccentric mass [20]. The intended final design would incorporate a smoother external profile with internal equatorial thrusters replacing the external thrusters, and wireless communication capability to replace the physical tether.

1.3.2. Spherical AUV Concepts

In 1984 Calvin Gongwer, of the Bendix Corporation, was issued a patent (US 4,455,962) for a spherical underwater vehicle concept [21]. The vehicle incorporates a single large propeller, of over half the size of the hull's maximum cross-sectional area, to propel the vehicle in the primary thrust direction. The vehicle can be further controlled with smaller tunnel thrusters mounted with axes parallel to the main propeller, distributed inside the outer perimeter of the sphere. Interestingly, the large propeller may be covered with a shroud to protect it during airborne deployment and subsequently automatically released at a pre-determined depth [21]. The large rear propeller would pose a significant entanglement hazard in the SIE environment.

The BYSQ-2, developed by Lan, Sun and Jia of China, ca. 2010, was actually prototyped for testing of its novel propulsion method [22]. The propulsion method consists of a single, vertical thruster mounted within the spherical hull. Attitude is adjusted via a weighted pendulum. The authors of [22] claim 6-DOF motion can be achieved via a "self-adaptive fuzzy logic" PID controller. This vehicle, although nearly perfectly smooth, lacks sufficient controllability for SIE.

Kim and Yu, of Korea proposed a novel spherical AUV concept in 2018 for the purpose of oceanographic field studies [23]. This design centered on modularity, with six cap-like "units" affixing to the sides of a central, watertight cube to form its spherical shape. Four thrusters, two of which are rotatable, would enable 4-DOF control, with the rotatable thrusters giving sway, heave, and yaw control and the fixed thrusters providing surge translation. The top and bottom units would provide environmental sensing instruments. Although the shape and size are appropriate and external protrusions are minimized, the design situates the thrusters close to the surface of the sphere, increasing the risk of entanglement. Full sensor coverage may also be difficult to achieve due to the large amount of exterior space dedicated to propulsion.

These interesting spherical AUV concepts all fall short of SIE capability due to entanglement and sediment disruption hazards (and controllability, in the case of the BYSQ-2).

1.3.3. Ultra-Compact AUVs

The Micro AUV (μAUV), developed by Watson et al. of the University of Manchester, UK (ca. 2011–2014) is intended as a low-cost, small-scale AUV for chemical pond monitoring [24]. Multiple μAUVs would be employed to establish a mobile underwater sensor network (MUSN) for this purpose. The prototype's hull incorporates two 150 mm diameter acrylic hemispheres, with a central, horizontal aluminum flange on which six external thrusters are mounted for 4-DOF (x, y, z, yaw) control [25]. The vehicle has been tested to a depth of 6 m and is powered by a single 7.4 v lithium-ion battery. On-board sensors include pressure, inertial gyro, and a magnetic compass.

The Omni-Egg, developed by Mazumdar et al. of Massachusetts Institute of Technology (MIT) (ca. 2012–2015) is a tetherless, spheroidal ROV designed for nuclear power

plant inspection [26–31]. The prototype is controlled via short-range radio communication. The spheroidal (egg-shaped), 3-D printed hull measures 146 × 108 mm and is hydrodynamically unstable in the yaw axis due to the Munk effect. The Munk effect describes the dynamic instability of a shape, such as a spheroid, moving longitudinally through the water [28]. One of the most notable features of this vehicle is its pump-jet propulsion system, which leverages the Coanda effect to reduce thrust-vectoring complexity via fluidic valves [31]. The Coanda effect describes the tendency of a water jet stream to move toward a path of lower pressure, which may be used to switch the jet from one path to another by opening or closing a port [31]. Propulsion is thus enabled with two such valves and one centrifugal pump. Positioning of the outlets enables 5-DOF (x, y, z, yaw, and limited pitch) control. An Arduino controller, camera and IMU are contained with the hull [26]. Notably, one iteration of the design incorporated a spherical hull of 106 mm diameter [29]. This vehicle was determined to behave with greater stability due to the absence of the Munk effect, however the spheroidal variants can leverage that same effect for increased turning agility [26].

The U-CAT, developed as part of the ARROWS project (described in Section 1.2) and tested in 2015 and 2016, is a biomimetic, spheroidal AUV designed specifically for the exploration of confined underwater spaces [2]. At a little over a half meter in length and 19 kg in weight, the U-CAT is significantly larger than the Omni Egg and resembles a sea turtle, propelling itself with four flippers, which pitch back and forth via four actuators. Buoyancy is controllable through a moveable piston. This propulsion design enables movement in 6-DOF within relatively tight spaces, and was also intended to reduce sediment disruption and entanglement susceptibility [2]. U-CAT carries a camera for internal compartment inspection and operates semi-autonomously, being hand-delivered to the wreck interior by a human diver, where it propagates through the structure along a pre-defined path. Other organic sensors include echo sounders, an acoustic beacon array, health monitoring sensors, a depth sensor, and an inertial measurement unit (IMU). The vehicle also houses an acoustic modem. Beacon aided navigation is possible thanks to its acoustic array, enabling movement through primarily restriction-free enclosed spaces [2].

The Amphibious Spherical Robot (ASRobot), developed by Xing et al. of China, ca. 2019, is a small but sophisticated autonomous vehicle capable of both swimming and crawling [32]. The turtle-inspired, 6.6 kg biomimetic device contains four legs, each terminating in a thruster, housed within a dual-hemispheric shell. The servo-driven legs consist of three joints, and enable a max crawl speed of 5.3 cm/s on land [32]. Organic sensors include a stereo camera, a pressure sensor array and an IMU. The vehicle also includes an acoustic modem for communication.

Each of these prototypes are highly maneuverable and small enough for SIE, but all are unsuited for the SIE mission due to the entanglement risk from external appendages (μAUV significantly, and U-CAT and ASRobot to a lesser extent) sediment disruption risk from horizontal or low-vectored wash (all vehicles), and significant payload limitations due to the small hull volume (especially Omni-Egg). U-CAT is the only vehicle designed for SIE capability, but requires a relatively obstruction-free environment to maneuver in [2].

1.3.4. Very Advanced/Commercial AUVs

Several large, highly sophisticated spherical (or spheroid) AUVs have been developed in recent years for operations in various extreme environments with greater maneuvering space than shipwreck interiors. DEPTHX, developed by Stone Aerospace Company of Texas, in partnership with the National Aeronautics and Space Administration (NASA) was developed from 2004–2007 for the exploration of underwater cenotes in Mexico [33]. A modified version of the vehicle, ENDURANCE, was later developed from 2008–2009 for the exploration of an ice-covered Antarctic lake [34]. The ENDURANCE mission was an analogue for the exploration of ice-covered lakes on Jupiter's moon, Europa. The IMOTUS-1 is an oil-rig inspection ROV, capable of autonomous operations [35]. The final version of the UX-1 (ca. 2020) is larger and far more advanced than its earlier prototype,

incorporating state-of-the-art sensing, such as laser-point-cloud based 3-D Simultaneous Localization and Mapping (SLAM) navigational techniques. DEPTHX and IMOTUS-1 use sonar-based SLAM.

1.3.5. Similar AUV Designs

The four vehicles described in this subsection are most similar to WIEVLE, the subject of this article. These vehicles span roughly two decades of development and vary greatly in sophistication. Each are spherical AUVs, and all (except for the early version of SUR, and UX-1) contain four thrusters. Each vehicle is also large enough to carry a significant sensor payload.

The spherical AUV Omni-Directional Intelligent Navigator (ODIN), was developed by Antonelli et al. at the University of Hawaii beginning in 1991 as an underwater control systems experimental platform [36–39]. By 2003, ODIN-III was outfitted with more advanced components, including a sensor suite of eight ranging sonars, an IMU and a depth sensor [36]. The basic hull, however, changed little over a decade of testing and consists of two hemispheres of machined aluminum 0.61–0.63 m in diameter with a max operating depth of 38 m. The vehicle is slightly positively buoyant at 125 kg, and 24 lead-gel batteries give the vehicle two hours of endurance and a max speed of 1 kt [37]. Eight externally mounted thrusters provide 6-DOF control.

The Spherical Underwater Robot (SUR), developed at Kagawa University, Japan, and Harbin University, China, (ca. 2011–2018) is a novel observation AUV incorporating pivoting water jet nozzles [40–52]. The 0.4 m diameter acrylic hull is a dual-hemisphere, free-flooding shell, joined at the equator with a flanged seam. The hull has large openings to allow for clearance with the moveable nozzles [40]. The earlier versions (SUR I and II) employed three jets, equally spaced and mounted on the points of an equilateral triangle mounted at the equator [41,52]. The later version, SUR III, added a fourth jet for increased maneuverability and efficiency in translation. The jets can be pivoted in both the vertical and horizontal planes, enabling 4-DOF (x, y, z, yaw) control [42,43]. Active yaw stabilization is required during translation. SUR III weighs 7.9 kg and has a max operating depth of 8 m. An IMU and pressure sensor facilitate feedback for control, and the latest version includes a Micron Data modem for potential networking of multiple vehicles [41].

Robador et al. developed a novel spherical AUV for nuclear power plant inspection ca. 2018 [53]. The AUV has a 30 cm diameter, dual-hemispheric, acrylic hull. Like SUR, the hull is free-flooding, with a water-tight enclosure in the center for housing electronics. Propulsion is enabled by four rotating, servo-driven, 90-degree waterjet nozzles quadrantally spaced around the equator (enabling active translation and yaw) with a central buoyancy compensation piston for passive vertical movement [53]. Onboard sensors include a pressure sensor, IMU, camera and LED ring.

The UX−1, developed by Fernandez et al. (ca. 2016), for the European Union's UNEXMIN Project, is a novel, spherical AUV designed for the exploration of flooded mines [54–60]. The early prototype was a smaller platform than the final, sophisticated version completed several years later (described earlier in this subsection). The UX-1 achieves 6-DOF control using eight internal tunnel thrusters and a rotating pendulum. Two cross-shaped manifolds house four thrusters each, integrated within the spherical, acrylic hull (diameter 0.6 m) symmetrically on opposite ends of the horizontal axis [60]. These thrusters provide x, y, and z translation as well as yaw and roll control. Pitch control is enabled by a moving pendulum weight incorporating the vehicle's batteries [58].

The four vehicles described in this final subsection come closest to SIE mission capability, but still fall short due to the restrictive nature of the interior environment. These capability gaps are shared with many of the other vehicles described earlier. Key hindrances to SIE capability include excessive size and weight, limited sensing capability, protruding components or gaps in the hull. Additionally, lack of upward thrust vectoring poses risk of sediment disturbance on the wreck interior structure.

The work presented in the remaining sections describes the design, control and early stage testing of an AUV prototype for SIE. Although WIEVLE shares some characteristics of many of the vehicles mentioned in this section, including its round, smooth hull and internal propulsion, it differs from each in its method of propulsion and sensor coverage. The resulting prototype, still very early in development, is a highly maneuverable, 4-DOF, spherical underwater vehicle, propelled by four fixed, symmetrical, angled internal tunnel thrusters. The authors contend that such a platform provides excellent maneuverability, with reduced risk of entanglement and sediment disruption within enclosed structures, and without the need for active control in the pitch and roll axes. Additionally, eliminating the need to rotate the vehicle for complete sensor coverage of the environment by integrating multiple cameras within the plated hull reduces mechanical complexity, as well as power consumption and environmental disturbances from unnecessary maneuvers.

2. Materials and Methods

2.1. Architecture Development Overview

The initial prototype, begun in the summer of 2018, was based on the conceptual design presented in [1]. The prototype, shown in Figure 1, is the product of multiple iterations of additive manufacturing, using polylactic acid (PLA), in combination with other relatively low-cost, commercial electronic components and standard, readily available materials such as polyvinyl chloride (PVC) and acrylonitrile butadiene styrene (ABS) tubing and stainless-steel fasteners.

(**a**) (**b**)

Figure 1. The Wreck Interior Exploration Vehicle (WIEVLE). (**a**) WIEVLE, on its test stand; (**b**) Plated hull removed to reveal WIEVLE's propulsion system.

The WIEVLE architecture addresses the key capability gaps of the vehicles addressed in Section 1.3, incorporating a novel, spherical hull and quad-core, internal tunnel thruster propulsion system to reduce the likelihood of entanglement and minimize sediment disturbance within the wreck interior environment. WIEVLE's four internal thrusters draw water from beneath the sphere and vector the propeller wash upwards and outwards, symmetrically, from the center. This flow path reduces downwash directed toward settled sediment beneath the sphere, in the same way cave divers, while executing proper technique, bend their legs and use tight, circular fin kicks, as shown in Figure 2a. The tunnel thruster configuration is depicted in the rendering of Figure 2b. The resultant force vectors, aligned axially with the outlet tubes, converge at the geometric center of the vehicle. This configuration enabled a stable hover during testing when the vehicle was ballasted for slight positively buoyancy (with no active thrust) at the surface. Center-of-gravity (CG)

and center-of-buoyancy (CB) were vertically separated for additional stability, particularly during translation.

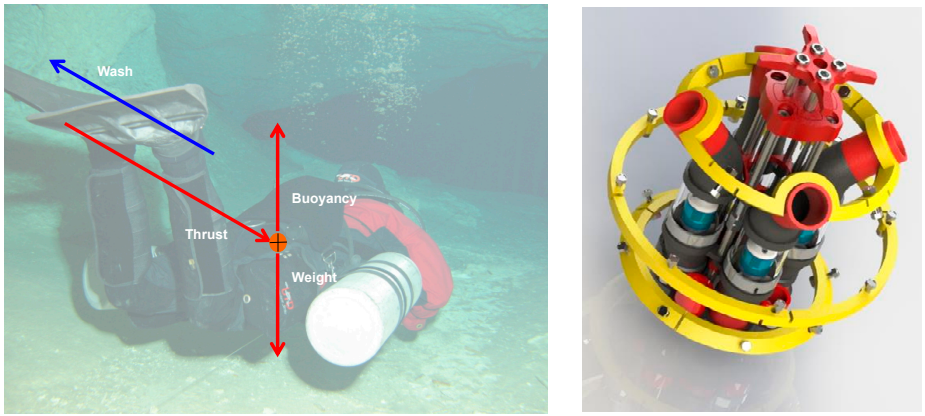

Figure 2. The inspiration behind the vehicle's angled thruster configuration (**a**) A cave diver, executing proper form [1] (**b**) A rendering of WIEVLE's quad-core propulsion system inside the plate retention rings.

To propagate, thrust is increased in any pair of adjacent thrusters, resulting in a corresponding increase in the combined lateral component of thrust. The vehicle's mass is distributed symmetrically to align the CG at or below the geometric center (GC) along the vertical axis. The vehicle is controlled by a single RaspberryPi 3B+ [61] (RPi) controller, running MATLAB SIMULINK software libraries for the RPi and Blue Robotics thrusters [62], implementing the control scheme described in Section 2.2. Each motor is powered by its own 14.8 v, 4000 mAH lithium polymer (LiPo) battery. To minimize entanglement, reduce the disruption of settled sediment and conserve battery power, maneuvers should be reduced to the minimum necessary for complete compartment sensor coverage. The propulsion system was designed to implement a 4-DOF navigation strategy. To achieve maximum sensor coverage while minimizing maneuvers, and their associated risk of entanglement or sediment disturbance, a plated, spherical hull was developed, as shown in Figure 3 to enable the placement of multiple cameras.

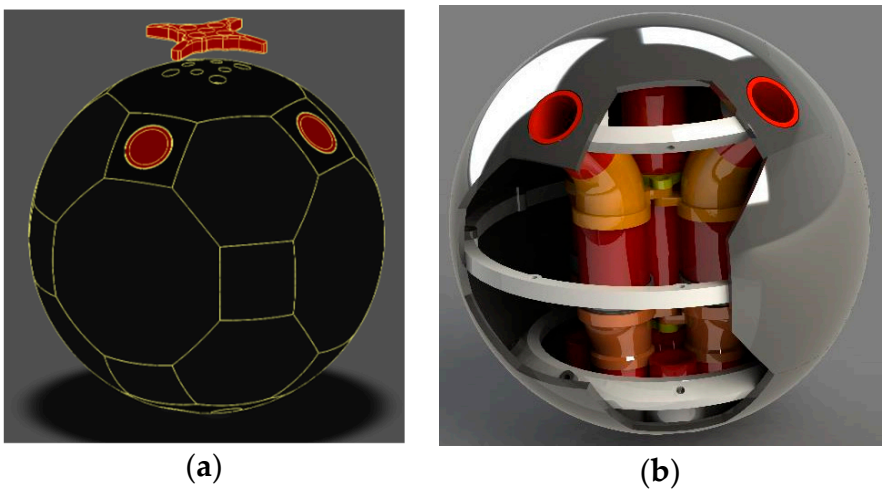

Figure 3. Renderings of WIEVLE's spherical, plated hull (**a**) Exterior plated hull (**b**) Individual plates are connected via plate retention rings.

The spherical, plated hull design has several advantages and disadvantages. First, the modular nature of the plate configuration makes the design ideal for mounting and

accessing sensors, enabling nearly complete (4π steradian) sensor and lighting coverage, thus satisfying the requirement to minimize rotational movements. Secondly, it enables the hull to be printed efficiently on common, less expensive 3-D printers. Rapid fabrication of the hull and propulsion core structural components can be achieved using printers with a relatively small print area, which may be of particular benefit to underway vessels with limited fabrication capability. Risk, in both time and expense, for damaged parts and failed prints is thereby reduced. A key disadvantage to a plated hull, however, is that the configuration and shape of the plates makes the hull very difficult to waterproof. The interior space of the current prototype is free flooding; thus, the plate rings can simply be stacked and are not required to withstand external pressure at depth. Additionally, alignment of the plates necessary to achieve a very smooth exterior is somewhat difficult. Additional payload space is available, via a central, vertical tube. Limited space is available elsewhere within the vehicle for essential components such as electronics, ballast containers and buoyancy foam.

2.2. Propulsion System Mechanics

WIEVLE is controlled by four rigid thrust tubes arranged symmetrically, radiating out from the center of the vehicle, as shown in Figure 4. In this section, for brevity, we will denote the center-of-gravity, center-of-buoyancy, and geometric center as G, B, and C, respectively. Note that the angles of the thruster tube outlets, which are arranged around the central payload tube cavity, are configured such that the four thrust vectors intersect at the geometric center of the vehicle (C). The analysis given in this section incorporates three key assumptions:

1. The vehicle is inherently positively buoyant (when no thrust is being produced).
2. Thrust vectors act in-line with the thrust tube axis.
3. The four 3-dimensional thrust vectors, $\vec{T}_1 \rightarrow \vec{T}_4$, can be reduced via vector addition to two vectors, $\vec{T}_{(1,2)}$ and $\vec{T}_{(3,4)}$ acting in two dimensions (the x-z plane), using the axis convention and numbering scheme depicted in Figure 4.

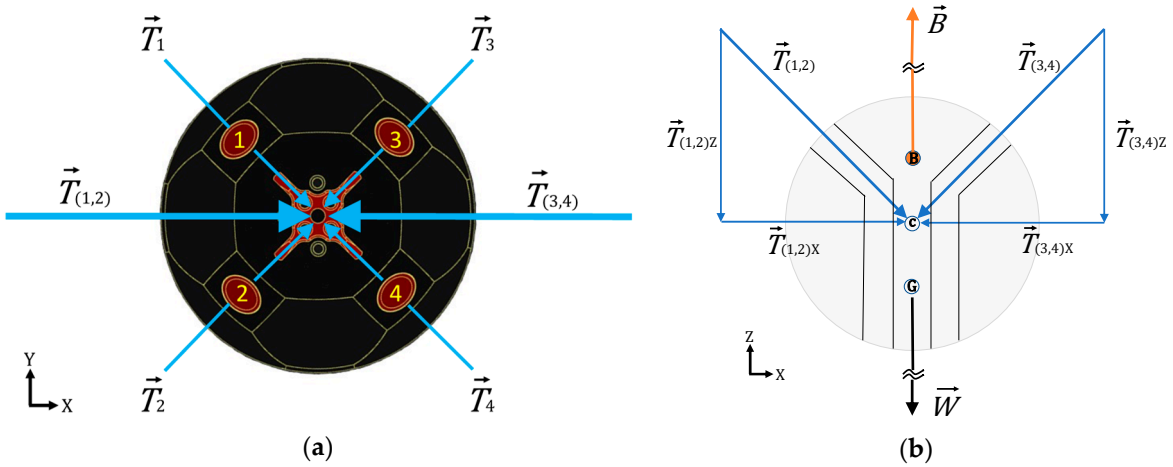

(**a**) (**b**)

Figure 4. Thrust vector summation for WIEVLE's four tunnel thrusters (**a**) Top view (**b**) Side view. Note the relative locations for B and G relative to C. These three key points are located along the central, vertical axis. The relative positions are depicted, but the precise distances and magnitudes of the vectors are unknown.

2.2.1. Hover Conditions

Let the UUV design characteristics (Equations (1)–(3)) enable the static conditions for a stable hover:

$$\sum F_X = 0 \rightarrow \vec{T}_{(1,2)x} = \vec{T}_{(3,4)x} \quad (1)$$

$$\sum F_Z = 0 \rightarrow \vec{B} - \vec{W} - \vec{T}_{(1,2)z} - \vec{T}_{(3,4)z} = 0 \tag{2}$$

$$\sum M_G = 0 \rightarrow \left(T_{(1,2)x} - T_{(3,4)x}\right) d_{(C \rightarrow G)z} = (0) d_{(C \rightarrow G)z} = 0 \tag{3}$$

where $d_{(C \rightarrow G)z}$ is the moment arm from the geometric center to the center-of-gravity and clockwise rotations about G are positive. In practice, the hover conditions of Equations (1)–(3) describe the state of the vehicle, fully submerged and under equal hovering thrust in each tube, such that the vehicle will be in a static, balanced state where no drift in the lateral ($x-y$) plane occurs, nor will depth change (z-axis) occur, since the vehicle's inherent positive buoyancy is equally offset by the sum of its weight and the downward, vertical components of the hover thrust ($\vec{T}_{(1,2)z} + \vec{T}_{(3,4)z}$). Additionally, no moments are produced about G, since the lateral components of thrust are equal and opposite.

Three cases for propulsion control protocols (increasing thrust to produce translation) can be identified. They are referenced in this work as follows: *unbalanced thrust* increase (Case 1), *balanced thrust* increase (Case 2) and co-located C and G with a *balanced thrust* increase (Case 3). Case 1, the simplest method, but with un-wanted rotational and translational characteristics, is described in Appendix A.1. Case 3, the ideal case from an energy standpoint, but with other significant drawbacks, is described in Appendix A.2. Case 2, a more refined approach than Case 1, and one that is easier to implement than Case 3, is the method currently employed on the prototype and is described in this section.

2.2.2. Case 2: The *Balanced Thrust* Increase

A *balanced thrust* increase is here defined as a proportional decrease in thrust for the thrusters directly opposite the pair in which thrust is increased. Referring to Figure 5, note that the total thrust produced by tubes 1 and 2 is $\vec{T}_{(1,2)} + \Delta\vec{T}_{(1,2)}$. The thrust from tubes 3 and 4 is reduced in equal proportion to the increase in thrust from tubes 1 and 2, hence (Equation (4)):

$$\vec{T\prime}_{(3,4)} = \vec{T}_{(3,4)} - \Delta\vec{T}_{(3,4)} \tag{4}$$

where $\vec{T\prime}_{(3,4)}$ is the reduced, combined thrust of tubes 3 and 4. $\vec{T}_{(1,2)} + \Delta\vec{T}_{(1,2)}$ and $\vec{T\prime}_{(3,4)}$ form the hypotenuse of similar right triangles, since the thrust tubes are symmetrically oriented within the sphere, therefore Equations (5) and (6) hold:

$$\Delta\vec{T}_{(1,2)x} = \Delta\vec{T}_{(3,4)x} = \Delta\vec{T}_x \tag{5}$$

$$\Delta\vec{T}_{(1,2)z} = \Delta\vec{T}_{(3,4)z} = \Delta\vec{T}_z \tag{6}$$

Now we examine the static force distribution for the *balanced thrust* profile (Equation (7)):

$$\begin{aligned} \sum F_X: \; & \vec{T}_{(1,2)x} + \Delta\vec{T}_{(1,2)x} - \vec{T\prime}_{(3,4)x} \\ &= \vec{T}_{(1,2)x} + \Delta\vec{T}_{(1,2)x} - \left[\vec{T}_{(3,4)x} - \Delta\vec{T}_{(3,4)x}\right] \\ &= \left[\vec{T}_{(1,2)x} - \vec{T}_{(3,4)x}\right] + \Delta\vec{T}_{(1,2)x} + \Delta\vec{T}_{(3,4)x} \\ &= [0] + 2\Delta\vec{T}_x = 2\Delta\vec{T}_x \end{aligned} \tag{7}$$

Note that the rearrangement yielded the term $\left[\vec{T}_{(1,2)x} - \vec{T}_{(3,4)x}\right]$, which is eliminated based on our hover specifications (Equation (1)), and the remainder is simplified by substitution according to Equation (5). Case 2 thus delivers twice the positive thrust to propel

the UUV in the $+x$ direction as Case 1 (see Appendix A.1). An examination of the vertical forces yields Equation (8):

$$\begin{aligned} \sum F_Z: \ & \vec{B} - \vec{W} - \vec{T}_{(1,2)z} - \vec{T\prime}_{(3,4)z} - \Delta\vec{T}_{(1,2)z} \\ &= \vec{B} - \vec{W} - \vec{T}_{(1,2)z} - \left[\vec{T}_{(3,4)z} - \Delta\vec{T}_{(3,4)z}\right] - \Delta\vec{T}_{(1,2)z} \\ &= \left[\vec{B} - \vec{W} - \vec{T}_{(1,2)z} - \vec{T}_{(3,4)z}\right] + \Delta\vec{T}_{(3,4)z} - \Delta\vec{T}_{(1,2)z} \\ &= [0] + \Delta\vec{T}_z - \Delta\vec{T}_z = 0 \end{aligned} \tag{8}$$

Once again, after rearrangement of terms and leveraging hover design specifications and symmetry, the result is good for Case 2; there is no unwanted net thrust in the vertical direction. Examining the moment about G yields Equation (9):

$$\begin{aligned} \sum M_G: \ & -\vec{T\prime}_{(3,4)x} d_{(C\to G)z} + \vec{T}_{(1,2)x} d_{(C\to G)z} + \Delta\vec{T}_{(1,2)x} d_{(C\to G)z} \\ &= d_{(C\to G)z}\left[-\vec{T\prime}_{(3,4)x} + \vec{T}_{(1,2)x} + \Delta\vec{T}_{(1,2)x}\right] \\ &= d_{(C\to G)z}\left[-\left(\vec{T}_{(3,4)x} - \Delta\vec{T}_{(3,4)x}\right) + \vec{T}_{(1,2)x} + \Delta\vec{T}_{(1,2)x}\right] \\ &= d_{(C\to G)z}\left[\left(\vec{T}_{(1,2)x} - \vec{T}_{(3,4)x}\right) + \left(\Delta\vec{T}_{(1,2)x} + \Delta\vec{T}_{(3,4)x}\right)\right] \\ &= d_{(C\to G)z}\left[(0) + \left(2\Delta\vec{T}_x\right)\right] \\ &= 2\Delta\vec{T}_x d_{(C\to G)z} \end{aligned} \tag{9}$$

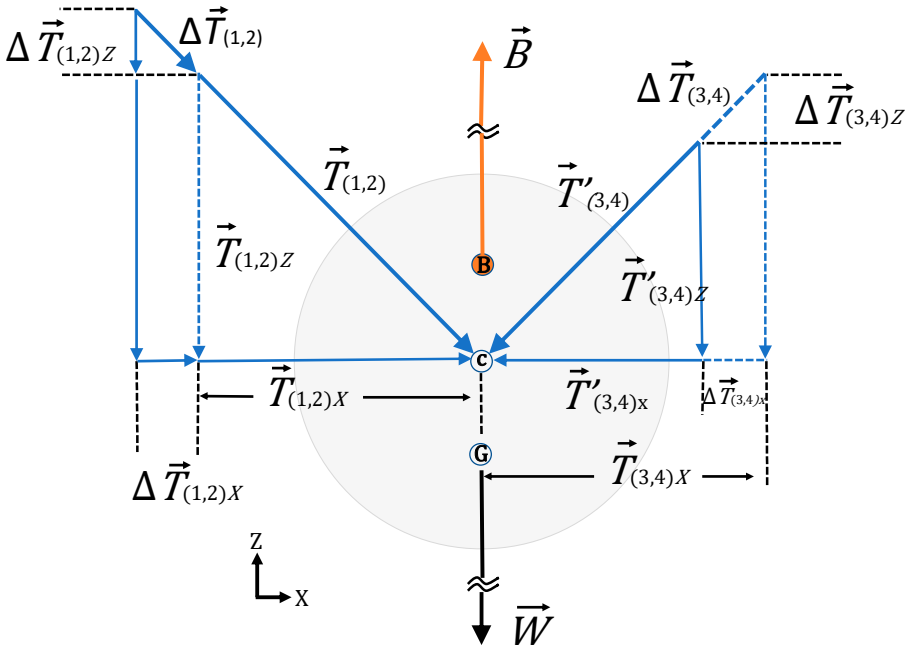

Figure 5. Case 2: *Balanced thrust* increase.

The cost of the improvements in Case 2, however, is a doubling (compared to Case 1) of the moment about G (Equation (9)). One may intuit a solution to this dilemma by ballasting the vehicle in order to co-locate C and G, thereby reducing $d_{(C\to G)z}$ to zero, and

eliminating the unwanted moment altogether. This approach to translation is described as Case 3 in the Appendix A.2. Case 3, however, requires ballasting that is difficult to achieve in practice and reduces the helpful righting moment that is especially useful in countering disturbances and un-wanted moments generated through changes in angular momentum, as will be discussed shortly.

For Case 2, the unbalanced torque will cause an initial rotation about G at some instance of time Δt shortly after a translational thrust command. The static force distribution at time $t + \Delta t$ is given in Figure 6.

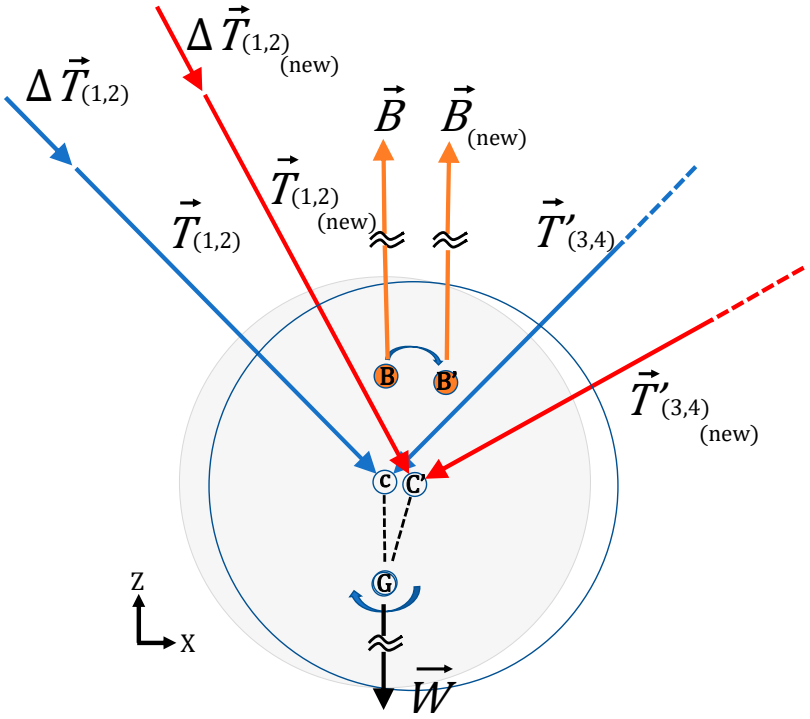

Figure 6. Case 2 $(t + \Delta t)$: *Balanced thrust* increase with resulting pitch.

The body of the sphere rotates clockwise about G. The new position of the geometric center and center-of-buoyancy are denoted as C′ and B′, respectively. Note the changes to the corresponding thrust vectors. $\vec{T}_{(1,2)} + \Delta\vec{T}_{(1,2)}$ is now less effective in generating $+x$ translation and more prone to pushing the sphere down, while $\vec{T\prime}_{(3,4)}$ has become less effective at pushing the sphere down and more effective at resisting $+x$ translation. The change in forces, from the reference frame of the sphere, is given in Figure 7.

Now let us examine the impact of this rotation on the static force distribution (Equation (10)):

$$\begin{aligned}
\sum F_X : & \left[\vec{T}_{(1,2)x} + \Delta\vec{T}_{(1,2)x} - \delta\vec{T}_{(1,2)x}\right] - \left[\vec{T}_{(3,4)x} - \Delta\vec{T}_{(3,4)x} + \delta\vec{T}_{(3,4)x}\right] \\
&= \left[\vec{T}_{(1,2)x} - \vec{T}_{(3,4)x}\right] + \left[\Delta\vec{T}_{(1,2)x} + \Delta\vec{T}_{(3,4)x}\right] - \delta\vec{T}_{(1,2)x} - \delta\vec{T}_{(3,4)x} \\
&= [0] + \left[2\Delta\vec{T}_x\right] - \delta\vec{T}_{(1,2)x} - \delta\vec{T}_{(3,4)x} \\
&= 2\Delta\vec{T}_x - \delta\vec{T}_{(1,2)x} - \delta\vec{T}_{(3,4)x}
\end{aligned} \tag{10}$$

Comparing Equation (10) to Equation (7), we see that the effectiveness of the net desired $(+x)$ thrust is reduced by the changes in thrust (acting in the $-x$ direction) due to the clockwise rotation of the thrust tubes. The rotation has caused the thrust from tubes 1

and 2 to become less effective at $+x$ propulsion, and tubes 3 and 4 to become more effective at resisting $+x$ propulsion. An examination of the new vertical forces yields Equation (11):

$$\begin{aligned}
&\sum F_Z: \ \vec{B} - \vec{W} - \left[\vec{T}_{(1,2)z} + \Delta\vec{T}_{(1,2)z} + \delta\vec{T}_{(1,2)z}\right] - \left[\vec{T}_{(3,4)z} - \Delta\vec{T}_{(3,4)z} - \delta\vec{T}_{(3,4)z}\right] \\
&= \left[\vec{B} - \vec{W} - \vec{T}_{(1,2)z} - \vec{T}_{(3,4)z}\right] + \left[-\Delta\vec{T}_{(1,2)z} + \Delta\vec{T}_{(3,4)z}\right] - \delta\vec{T}_{(1,2)z} + \delta\vec{T}_{(3,4)z} \\
&= [0] + [0] - \delta\vec{T}_{(1,2)z} + \delta\vec{T}_{(3,4)z} \\
&= -\delta\vec{T}_{(1,2)z} + \delta\vec{T}_{(3,4)z}
\end{aligned} \tag{11}$$

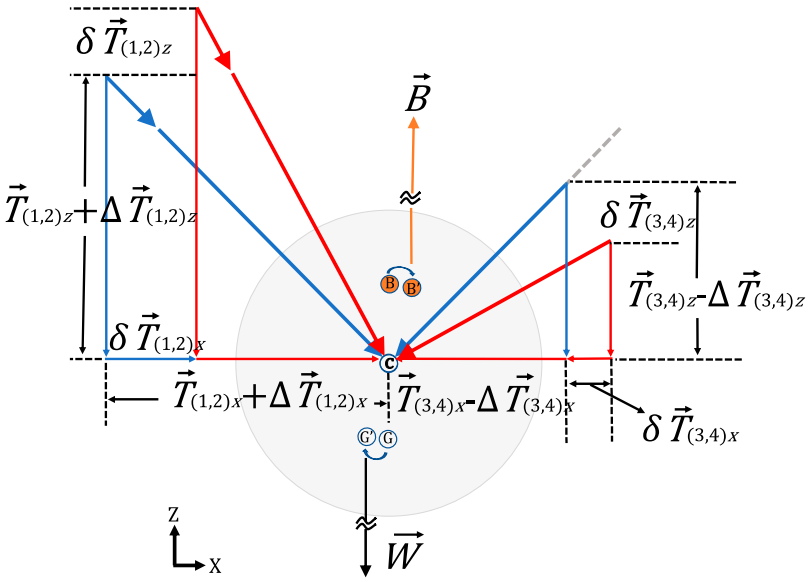

Figure 7. Case 2 ($t + \Delta t$): *Balanced thrust* increase (post induced pitch).

An undesirable thrust change has occurred in the z axis, albeit smaller in magnitude than the change in the x axis. Finally, an examination of the moments about G′ gives Equation (12):

$$\begin{aligned}
&\sum M_{G'}: \ -\vec{B}d_{(B'\to G')x} + \left[\vec{T}_{(1,2)z} + \Delta\vec{T}_{(1,2)z} + \delta\vec{T}_{(1,2)z}\right]d_{(C\to G')x} + \left[\vec{T}_{(3,4)z} - \Delta\vec{T}_{(3,4)z} - \delta\vec{T}_{(3,4)z}\right]d_{(C\to G')x} \\
&\ldots + \left[\vec{T}_{(1,2)x} + \Delta\vec{T}_{(1,2)x} - \delta\vec{T}_{(1,2)x}\right]d_{(C\to G')z} - \left[\vec{T}_{(3,4)x} - \Delta\vec{T}_{(3,4)x} + \delta\vec{T}_{(3,4)x}\right]d_{(C\to G')z} \\
&= -\vec{B}d_{(B'\to G')x} + \left[\vec{T}_{(1,2)z} + \Delta\vec{T}_{(1,2)z} + \delta\vec{T}_{(1,2)z} + \vec{T}_{(3,4)z} - \Delta\vec{T}_{(3,4)z} - \delta\vec{T}_{(3,4)z}\right]d_{(C\to G')x} \\
&\ldots + \left[\vec{T}_{(1,2)x} + \Delta\vec{T}_{(1,2)x} - \delta\vec{T}_{(1,2)x} - \vec{T}_{(3,4)x} + \Delta\vec{T}_{(3,4)x} - \delta\vec{T}_{(3,4)x}\right]d_{(C\to G')z} \\
&= -\vec{B}d_{(B'\to G')x} + \left[\vec{T}_{(1,2)z} + \vec{T}_{(3,4)z} + \left(\Delta\vec{T}_z - \Delta\vec{T}_z\right) + \delta\vec{T}_{(1,2)z} - \delta\vec{T}_{(3,4)z}\right]d_{(C\to G')x} \\
&\ldots + \left[\left(\vec{T}_{(1,2)x} - \vec{T}_{(3,4)x}\right) + \left(2\Delta\vec{T}_x\right) - \delta\vec{T}_{(1,2)x} - \delta\vec{T}_{(3,4)x}\right]d_{(C\to G')z} \\
&= -\vec{B}d_{(B'\to G')x} + \left[\vec{T}_{(1,2)z} + \vec{T}_{(3,4)z} + \delta\vec{T}_{(1,2)z} - \delta\vec{T}_{(3,4)z}\right]d_{(C\to G')x} \\
&\ldots + \left[\left(2\Delta\vec{T}_x\right) - \delta\vec{T}_{(1,2)x} - \delta\vec{T}_{(3,4)x}\right]d_{(C\to G')z}
\end{aligned} \tag{12}$$

Complexity has increased somewhat due to the introduction of a second moment arm $d_{(C\to G')x}$. Three key implications can now be identified. First, the magnitude of the weight has no direct influence on the sum of the moments about G′, as it will always

act through G′. Second, buoyancy generates the corrective moment (counterclockwise in this case), countering the positive (clockwise) moment produced by $\Delta\vec{T}_x$. This corrective moment increases as the vehicle pitches; therefore, a strong buoyancy force is desirable. Furthermore, the greater the vertical separation of B from G, the greater the moment arm produced during an unwanted pitch $d_{(B'\to G')x}$. A strong buoyancy force is a desired design specification, addressed during the design conditions for the stable hover. $\vec{B}$ may be increased in concert with either a corresponding increase in $\vec{W}$ or collective thrust $\vec{T}_{(1,2)} + \vec{T}_{(3,4)}$ in order to maintain vertical equilibrium in a hover. Additionally, recalling Case 3, the moment that produces the unwanted pitch can be eliminated altogether by reducing $d_{(C\to G)z}$, (Equation (9)) to zero by co-locating C and G. This can be achieved independent of a strong (and vertically separated) B.

2.2.3. Angular Momentum, Yaw Control and Drag

The conservation of angular momentum is of concern whenever a vehicle incorporates rotating components. The direction of rotation of individual thrusters is depicted in Figure 8.

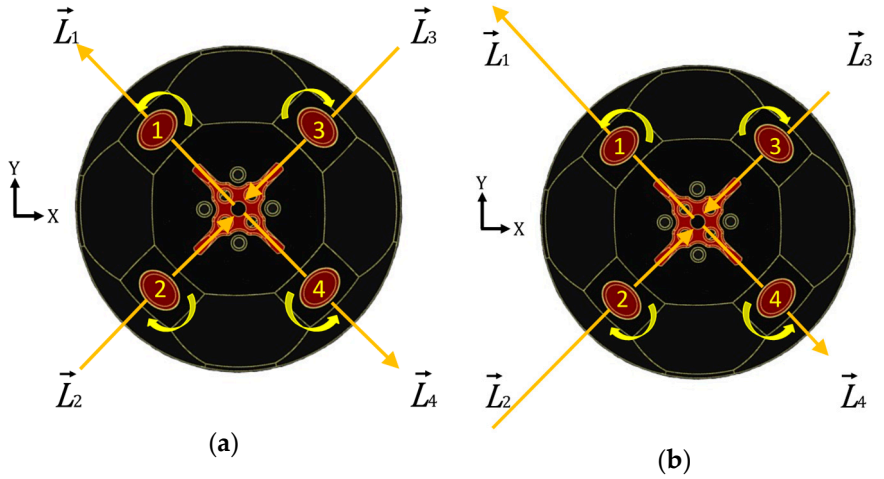

Figure 8. Angular momentum (top view) (**a**) Hover conditions (**b**) *Balanced thrust* increase for $+x$ translation. Note the thrusters are arranged with counter-rotating spins (yellow arrows), necessary to prevent unintended yaw due to conservation of angular momentum. Additionally, note the orientation of the corresponding angular momentum vectors (orange).

An examination of the angular momentum associated with a hover state (Figure 8a) gives Equation (13):

$$\begin{aligned} \vec{L}_1 &= -\vec{L}_{(1)x} + \vec{L}_{(1)y} + \vec{L}_{(1)z} \\ \vec{L}_2 &= \vec{L}_{(2)x} + \vec{L}_{(2)y} - \vec{L}_{(2)z} \\ \vec{L}_3 &= -\vec{L}_{(3)x} - \vec{L}_{(3)y} - \vec{L}_{(3)z} \\ \vec{L}_4 &= \vec{L}_{(4)x} - \vec{L}_{(4)y} + \vec{L}_{(4)z} \end{aligned} \tag{13}$$

Let $L_1 = L_2 = L_3 = L_4 = L$, then the sum of the angular momentum gives Equation (14):

$$\begin{aligned} \sum \vec{L} &= \sum_1^4 [L_x + L_y + L_z] \\ &= (-L + L - L + L) + (L + L - L - L) + (L - L - L + L) = 0 \end{aligned} \tag{14}$$

A *balanced thrust* increase for $+x$ translation will increase the angular momentum of tubes 1 and 2 and decrease the angular momentum of tubes 3 and 4 by a magnitude

ΔL, where $\Delta L_1 = \Delta L_2 = \Delta L_3 = \Delta L_4 = \Delta L$. An examination of the angular momentum associated with a *balanced thrust* increase (Figure 8b) gives Equation (15):

$$\begin{aligned}
\vec{L_1} &= -\vec{L}_{(1)x} + \vec{L}_{(1)y} + \vec{L}_{(1)z} = -\left(\vec{L} + \vec{\Delta L}\right)_{(1)x} + \left(\vec{L} + \vec{\Delta L}\right)_{(1)y} + \left(\vec{L} + \vec{\Delta L}\right)_{(1)z} \\
\vec{L_2} &= \vec{L}_{(2)x} + \vec{L}_{(2)y} - \vec{L}_{(2)z} = \left(\vec{L} + \vec{\Delta L}\right)_{(2)x} + \left(\vec{L} + \vec{\Delta L}\right)_{(2)y} - \left(\vec{L} + \vec{\Delta L}\right)_{(2)z} \\
\vec{L_3} &= -\vec{L}_{(3)x} - \vec{L}_{(3)y} - \vec{L}_{(3)z} = -\left(\vec{L} - \vec{\Delta L}\right)_{(3)x} - \left(\vec{L} - \vec{\Delta L}\right)_{(3)y} - \left(\vec{L} - \vec{\Delta L}\right)_{(3)z} \\
\vec{L_4} &= \vec{L}_{(4)x} - \vec{L}_{(4)y} + \vec{L}_{(4)z} = \left(\vec{L} - \vec{\Delta L}\right)_{(4)x} - \left(\vec{L} - \vec{\Delta L}\right)_{(4)y} + \left(\vec{L} - \vec{\Delta L}\right)_{(4)z}
\end{aligned} \tag{15}$$

Thus, the sum of the angular momentum for all four thrusters gives Equation (16):

$$\begin{aligned}
&\sum \vec{L} = \sum_{1}^{4}\left[\vec{L}_x + \vec{L}_y + \vec{L}_z\right] \\
&= \left[-\left(\vec{L} + \vec{\Delta L}\right)_{(1)} + \left(\vec{L} + \vec{\Delta L}\right)_{(2)} - \left(\vec{L} - \vec{\Delta L}\right)_{(3)} + \left(\vec{L} - \vec{\Delta L}\right)_{(4)}\right]_x + \ldots \\
&\left[\left(\vec{L} + \vec{\Delta L}\right)_{(1)} + \left(\vec{L} + \vec{\Delta L}\right)_{(2)} - \left(\vec{L} - \vec{\Delta L}\right)_{(3)} - \left(\vec{L} - \vec{\Delta L}\right)_{(4)}\right]_y + \ldots \\
&\left[\left(\vec{L} + \vec{\Delta L}\right)_{(1)} + \left(\vec{L} + \vec{\Delta L}\right)_{(2)} - \left(\vec{L} - \vec{\Delta L}\right)_{(3)} - \left(\vec{L} - \vec{\Delta L}\right)_{(4)}\right]_y + \ldots \\
&= 0 + 4\vec{\Delta L}_y + 0 = 4\vec{\Delta L}_y
\end{aligned} \tag{16}$$

The *balanced thrust* increase can thus be shown to induce an unwanted rotation-inducing moment about the y-axis, due to the conservation of angular momentum. Applying the right-hand rule, we can determine that a downward pitching moment would be induced in this case. A similar examination of angular momentum, given *balanced thrust* translation in the $-x$, $+y$ and $-y$ directions, yields a similar magnitude of angular momentum ($4\Delta L$), inducing "backward" pitch, and "right" and "left" roll, respectively (given a vehicle reference frame with $+x$ as "forward"). This moment must be overcome with a sufficiently strong righting moment generated through ballasting. Early translation testing demonstrated that this was easily achievable, even in a free-flooding hull offering limited space for buoyancy foam.

Despite the capability for full sensor coverage due to the hull configuration, yaw authority (unlike pitch and roll authority) is very important for efficient navigation. Without such control, the vehicle could still achieve sensor coverage of a given compartment, but it would have to navigate from point-to-point in an inefficient, step-wise manner (i.e., executing a series of movements along the principle axes of the body frame of reference in order to navigate to an off-axis location, rather than taking a direct path to the target waypoint). Similarly, heading changes due to disturbances would complicate the navigation path. Fortunately, conservation of angular momentum also enables yaw command authority by changing the relative thrust of either of the two sets of opposed thrusters, in the same manner as standard aerial quad-copter yaw control. A similar examination of angular momentum, as described by Equations (15) and (16), yields a left (counterclockwise) yaw with an increase in thrust (and corresponding $+\vec{\Delta L}$) in tubes 1 and 4 and a corresponding decrease in thrust in tubes 2 and 3. A clockwise rotation can be shown to occur with the increasing of the thrust in the opposite pair of tubes. Tethered testing demonstrated positive yaw authority despite the angled nature of the thrust tubes. As in the case with translation, a balanced approach (proportional increase in thrust in one pair and decrease in another) is necessary to maintain depth.

After movement through the water has begun, the resistance of the water will cause a pressure increase on the half of the sphere facing the relative incoming flow. Due to its symmetry, the pressure distribution can be approximated to a single opposing, axial

drag force vector acting at the center-of-pressure, which can also be extended through the geometric center. In Case 3 (Appendix A.2), where C is co-located with G, this drag force will not generate a moment about G. In Case 2, the drag-induced moment must also be mitigated by the righting moment. Given WIEVLE's relatively slow transiting speeds, drag-induced moments are not difficult to overcome. Testing of the prototype, discussed in Section 3, demonstrated that a traditional ballasting scheme (achieving a low G by adding lead shot cannisters to the base, and a high B, by adding marine expanding foam at the top), provided excellent stability in both hover and translation.

2.3. Architecture

2.3.1. Spherical Hull

The exploration of shipwreck compartments constrains the maximum hull diameter to roughly the size of a basketball. The Makerbot Replicator Z18 3-D printer has a maximum print area of approximately this size (approximately 30 × 30 cm); thus, the first full-scale (29.85 cm diameter), hemispheric print, as shown in Figure 9a, was completed using this machine.

(**a**) (**b**)

Figure 9. Hemispheric and plated spherical hulls (**a**) Initial 1/4-scale model and full-scale, hemispheric hull prototypes (**b**) Plated hull configuration.

The combined print time for both hemispheres exceeded 117 h (at 6 mm thickness, 25% infill) using 1.4 kg of black PLA. Long hemispheric print times, combined with some structural flaws, led to the abandonment of the hemispheric concept and redesign of the hull using the plated-ring scheme described in Section 2.1, as shown in Figure 9b. An additional fabrication benefit to the plated-ring approach is that multiple plates and retention ring segments can be printed flat (oriented such that the outer surface of the sphere is on top). This resulted in a finer finish when using support material, and enabled the use of smaller printers, which was a design goal. Additionally, all areas of the hull appeared to be stronger when printed as plates than when printed as hemispheres—particularly for the hull sections near the equator. At 20% infill, one of the large equatorial ring plates can be printed in just under 12 h on an Ultimaker 2+.

The assembled hull—a truncated cuboctahedron—consists of 26 plates, including eight small hexagons, 12 small squares, and six large octagons arranged on three rings between the upper and lower plates, as shown assembled in Figure 9b. The individual plates are connected to three yellow plate retention rings by stainless steel fasteners. The lower plate ring is similar to the upper plate ring, except that it does not contain thruster outlets. The equatorial ring contains larger plates, which may be exchanged for plates specially designed for integrating sensors such as cameras, as described in Section 2.3.2. The three plate rings are held together between the top and bottom plates, shown in Figure 10. Each plate ring stacks from the bottom up, and is held in position by the central retention bolts.

(a) (b)

Figure 10. Top and bottom hull plates (**a**) Top plate, displaying the four circular retention bolt heads, with the carry handle removed (**b**) Bottom plate, displaying the hexagonal bolt heads, thruster inlets and (empty) ballast and central payload tube ports.

The bottom plate includes four thruster tube inlets, an access port for the central payload tube, and four smaller access ports for the ballast canisters. The ballast canisters have threaded caps which can be accessed externally to adjust quadrant list with the addition of lead shot. All hull plates and rings were lightly sanded and coated with clear polyurethane varnish to reduce the rate of water penetration and corresponding buoyancy change when submerged.

2.3.2. Ballast and Payload

Figure 11 depicts the placement of buoyancy foam within the free-flooding sphere to achieve a stable orientation and ensure net positive buoyancy.

(a) (b)

Figure 11. Buoyancy foam installation (**a**) Hard, closed cell foam pieces are inserted between the hull and battery tubes. Note the small water-tight cannister in the central cavity contained the power supply for the controller for use during testing. (**b**) Marine expanding foam under the top plate contributes to a high center-of-buoyancy.

The first sensors to be integrated with the prototype were four GoPro Hero Session 5 cameras, as shown in Figure 12. The cameras are factory waterproof to moderate depths and ideally shaped to enable the lens to sit flush with the surface of the sphere for a wide field-of-view. Thus, with a camera in each quadrant, WIEVLE can record much of its environment without rotational maneuvers.

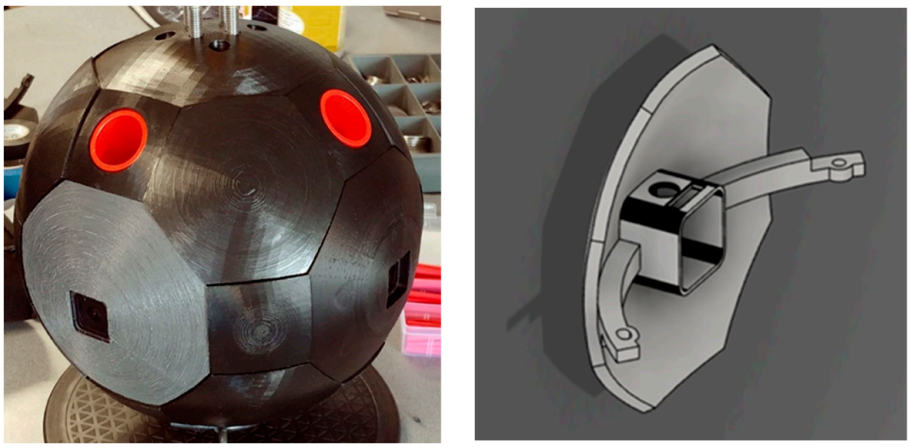

(a) (b)

Figure 12. Camera payload configuration (**a**) Equatorial ring modified to carry four GoPro Hero Session 5 cameras (**b**) Render of equatorial plate configured for camera integration.

2.3.3. Propulsion and Electronic Control

The propulsion system consists of a core of four thrust tubes, held in place by the retention bolts, which pass through offset and interlocking loops on each of the printed upper and lower thruster tube ducts. This results in a sturdy propulsion core, as seen in Figure 13.

(a) (b)

Figure 13. Propulsion core (**a**) Oblique (**b**) Top-down view. Note the four lower retention bolts capped by coupling nuts, which will join with the four upper bolts. Batteries and buoyancy foam are removed.

Four hex head stainless-steel retention bolts insert upwards from the bottom plate, through the loops of the lower and upper thrust tube ducts and join with four coupling nuts. Four shorter socket head bolts are inserted through the top plate and join with the coupling nuts from above. Thus, each layer of the propulsion core tubing stacks above the next, held in position by these four retention bolts. The lower four hex heads are counter-sunk in hexagon holes within the lower plate to prevent rotation during tightening, while the upper four socket cap heads are countersunk in circular holes to enable rotation. With this configuration, the four bolts retaining the upper plate can be removed, and each plate ring subsequently lifted off, for easy access to the internal components. To enable secure and convenient handling of the vehicle, a detachable yellow a carry handle, depicted in Figure 13, was designed to screw into the top plate, ensuring that the lifting force is transferred through the core.

Four Blue Robotics M100 motors, controlled by a Raspberry Pi 3B+ controller, are mounted inside acrylic tubes, as shown in Figure 13a. As previously mentioned, each thruster was powered by its own 14.8 v lithium polymer battery within watertight ABS

containers during testing, as depicted in Figure 11a. Custom printed propellers were designed with a reduced nosecone compared to the stock propellers in order to reduce constriction of the limited cross-sectional area of the flow and maximize blade surface. PVC inlet tubes expand via printed ducting before the motors, such that a constant cross-sectional area of the flow is maintained around the motors, before being reduced again with printed ducts at the top of the acrylic tubes prior to the PVC outlet tubes. Each electrical component, other than the waterproof M100s and cameras, are either housed in a custom watertight container or encased in marine resin.

3. Initial Testing

The goal of the initial laboratory testing was to demonstrate the proposed propulsion method and make some preliminary observations of the prototype's construction. In typical, progressive test and evaluation fashion, individual subsystems were first assembled and water-proofed, then tested individually while submerged, before the first fully integrated, ballasted functional testing of the vehicle was conducted, as shown in Figure 14.

(**a**) (**b**)

Figure 14. First fully integrated, ballasted test of the vehicle (**a**) Initially, foam insulation pieces were packed tightly inside the sphere to provide buoyancy. (**b**) Quadrant list was relieved in the early "bucket tests" with the addition of lead shot cannisters in the bottom plate's ballast ports.

The initial testing was conducted in the wave-generator test facility at the Naval Postgraduate School, as shown in Figure 15. These tests, conducted by systems engineering students as part of their master's capstone course, incorporated simple, open-loop maneuver profiles uploaded wirelessly to the controller prior to submersion. The capstone team recorded highlights of the early testing in a video provided as a supplement to this article [S1]. The SIMULINK profiles commanded basic maneuvers, such as hovering, diving and horizontal translation. Without sensor feedback, autonomous depth and heading control is not yet possible, but the objective of these first tests was simply to prove that the vehicle could be commanded to translate, dive, surface and yaw while maintaining a stable, upright orientation. Prior to each test run, a profile was uploaded wirelessly to the Raspberry Pi from a bench laptop while the vehicle was above the surface and capable of receiving communications. Once loaded, the vehicle, ballasted and secured for diving, was lowered into the water, floating just below the surface. After each profile was executed, WIEVLE would float back up to the surface. WIEVLE executed short vertical and horizontal propagation runs in these first un-tethered, open-loop controllability tests, maintaining good stability (only minor transient pitch and roll).

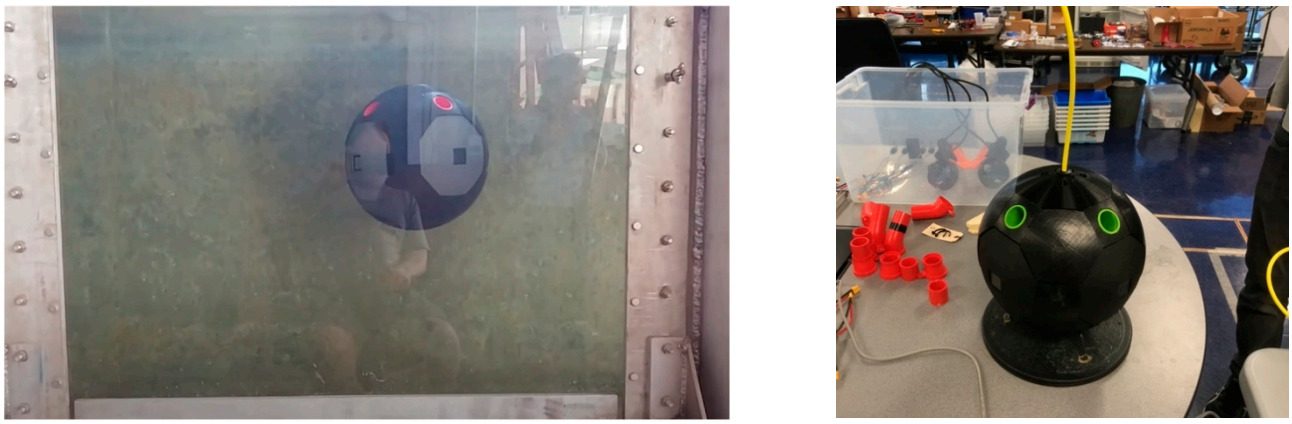

(**a**) (**b**)

Figure 15. WIEVLE testing (**a**) Initial open-loop, untethered tank testing (**b**) Modified hull for tethered testing.

With the vehicle's translational stability thus qualitatively demonstrated, and in order to more rapidly test various maneuvers, a lightweight tether was installed through the center of the top plate for subsequent tests, temporarily replacing the onboard Raspberry Pi controller in order to manually control individual thrusters from a nearby control station. Yaw control was first demonstrated during tethered testing, also with satisfactory vertical stability.

Quantitative data, demonstrating key performance characteristics such as maximum translation speed, endurance, and depth changing or holding capability, has not yet been collected, and at this early stage of development, the authors make no claim to specific performance characteristics. Further testing is necessary to collect this and other key performance data, such as settling times, after the development of a suitable controller and the integration of a depth sensor and IMU for closed-loop testing. Follow-on experiments should also test the key aspects of SIE-capability; for example, the ability to pass near sediment-covered structures with minimal disturbance, transit through entanglement hazards, and, eventually, autonomously navigate through simulated wreck interiors.

Qualitatively, the simple (albeit limited) tests conducted to date, both with and without a tether, generally confirm the expected propulsion behavior (open-loop translation capability in x, y, z and yaw). Most significantly, stability was demonstrated during all maneuvers, relieving fears of the small, smooth sphere tumbling when thrust was applied (especially during translation), as the vehicle's inherent stability kept it upright with only minor, transient oscillations in pitch and roll. The M100 thrusters, with their custom propellers, also produced significant thrust—capable of driving the slightly buoyant vehicle quite soundly into the floor of the four-foot-deep tank. The hull and internal support structure appear sufficiently strong for practical operations in and out of the water, although areas for structural improvement were identified.

4. Discussion

WIEVLE is offered in this article as a potential AUV design solution toward the challenge of shipwreck interior exploration and other confined, entanglement-prone underwater environments. The SIE mission was defined, and historic examples demonstrating its value were given. Traditional and modern approaches to shipwreck survey were then introduced, followed by a review of prior work in confined-space underwater vehicle designs. The conceptual design of WIEVLE was then described, with emphasis on the SIE-related capability gaps of prior vehicles, followed by a detailed description of the propulsion mechanics and the prototype construction. Finally, the limited, initial testing of the vehicle was described, along with recommended future tests.

WIEVLE's defining design characteristics, and corresponding motivations, can thus be summarized as:

1. *A smooth, spherical exterior hull* to reduce the hazards of entanglement while providing symmetry in both hardware layout and propulsion mechanics, since approximately equal resistance is experienced in any direction as the vehicle moves through the water, unlike asymmetric or non-spherical shapes likes spheroids, traditional, torpedo-shaped or square-hulled UUVs, or those with external projections such as thrusters or fins. A spherical vehicle can rotate in place with no change in the volume of space encompassing this movement.
2. *4-DOF maneuver capability*, to enable movement in tight spaces while remaining in a stable, upright orientation.
3. *Multiple cameras installed around the hull*, to enable compartment exploration with minimal maneuvers.
4. *Fixed, upward-angled tunnel thrusters* to direct propeller wash up and away from the majority of settled sediment within the wreck structure, especially sediment near the elevation of the vehicle.

5. Future Work

The immediate development priority for WIEVLE is the attainment of autonomous navigation capability through the design of a suitable controller. Three key challenges for controlling the underactuated AUV are given in [63]: (1) non-linear dynamics, (2) model parameter uncertainty and (3) external disturbances, all of which apply to this vehicle. Many types of control strategies for underactuated vehicles are described in [63]. WIEVLE, operating with 4-DOF, potentially under strong currents and at risk of unpredictable events, may be considered underactuated. Unforeseeable internal anomalies, such as the loss of a motor, or external anomalies or perturbations, such as the encountering of an eddy current, collision with structure or impact from falling debris or sea life, can cause an unpredicted shift in trajectory. The controller must autonomously adapt to such disturbances in an actual SIE mission. A recent approach to this problem involves the application of Deterministic Artificial Intelligence (DAI) applied to the trajectory of an the AUV [64]. The SIE environment necessitates flexible autonomy once the vehicle enters the interior space and outside communication is impossible. Such a self-awareness capability would, therefore, be highly desirable.

Simultaneously, new payloads for the equatorial ring and central payload tube should be explored. Offset lighting is currently being integrated with the plate rings to augment the cameras. Additional improvements currently underway include a parallel battery configuration with improved safety features, upgraded battery and electronic housings, a more rigid propulsion core and modular 3-D printed buoyancy chambers to replace the existing expanding foam. One approach to a navigational method for the exploration of multiple compartments or complex spaces is the use of the central payload tube for beacon-aided navigation, as discussed in detail in [1,65]. By deploying beacons as it travels, WIEVLE could establish a "bread crumb trail" communications network, such as that described in [66], thereby reducing mission risk by enabling outside communication with the vehicle when inside the wreck and simultaneously providing a means for the vehicle to find its way back out of the structure. Finally, the central payload tube, or adjacent ports, could be used to contain an active buoyancy control mechanism, such as described in [1,67] and implemented in [53], reducing power requirements and environmental disturbance during maneuvers.

6. Patents

U.S. Application No. 62/903,534 filed 20 September 2019.

Author Contributions: Conceptualization, R.E.; methodology, R.E. and J.L.; software, J.L.; validation, R.E.; formal analysis, R.E.; investigation, R.E.; resources, R.E. and A.P.; data curation, R.E.; writing—original draft preparation, R.E.; writing—review and editing, R.E., J.L. and A.P.; visualization, R.E.; supervision, R.E.; project administration, R.E.; funding acquisition, R.E. and A.P. All authors have read and agreed to the published version of the manuscript.

Funding: This research was funded by the Consortium for Robotics and Unmanned Systems Education and Research (CRUSER) at the U.S. Naval Postgraduate School in Monterey, CA, USA.

Institutional Review Board Statement: Not applicable.

Informed Consent Statement: Not applicable.

Data Availability Statement: Not applicable.

Acknowledgments: Jonathan Lussier, NPS summer intern (2018) and co-inventor, was instrumental to this project's success. He designed the initial CAD model for the vehicle and tirelessly assisted with many other aspects of the prototype's construction, including printing, wiring and waterproofing components. Anthony Pollman provided very valuable guidance in the application for and administration of research funds. Noah Gomes, NPS volunteer summer intern (2019, 2020), assisted the effort by documenting the original electrical wiring and developing an alternative battery design. Navy lieutenants Chris Diaz, Marcy Herster-Dudley, Chris Hevey, Josh Hildebrand, Katy Irgens, Andrew Miller and Beth Rajchel—2020 M.S. in Systems Engineering graduates of the Naval Postgraduate School and students of the SE3201–3 Engineering Systems Conceptualization, Design, Implementation and Operation capstone course sequence—were instrumental in the development of the camera payload ring, ballast, early controller programming, network setup and initial testing of the vehicle. I wish them the very best in their Naval careers. Finally, Chris Clay, Faculty Associate—Research at the Naval Postgraduate School, has been extraordinarily helpful in the design and construction of excellent new improvements to the original version of the vehicle, described in this paper. I look forward to continuing our work together.

Conflicts of Interest: The authors declare no conflict of interest.

Appendix A

Appendix A.1. Case 1: Unbalanced Thrust Increase

Let us command a level translation in the $+x$ direction by increasing the thrust in tubes 1 and 2 ($\vec{T}_{(1,2)}$) without changing the thrust in tubes 3 and 4, as depicted in Figure A1.

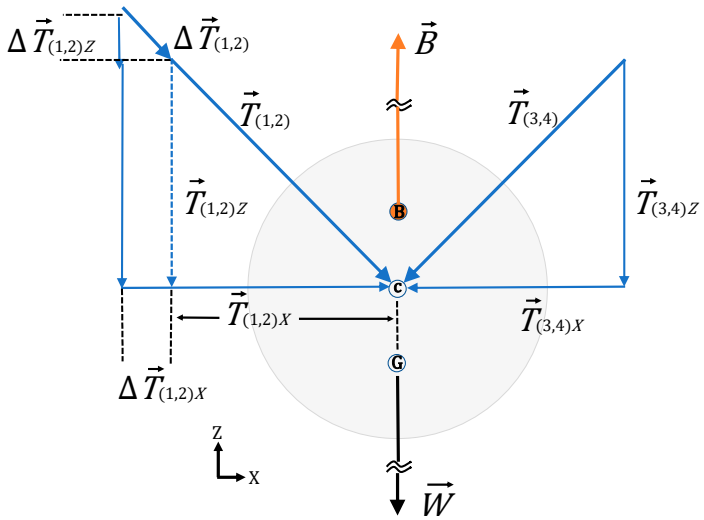

Figure A1. Case 1: *Unbalanced thrust* increase.

Examining the forces in the x direction gives Equation (A1):

$$\sum F_X: \ \vec{T}_{(1,2)x} + \Delta\vec{T}_{(1,2)x} - \vec{T}_{(3,4)x} = \Delta\vec{T}_{(1,2)x} \tag{A1}$$

A positive force is generated to propel the vehicle in the $+x$ direction. An examination of the z-axis gives Equation (A2):

$$\sum F_Z: \left[\vec{B} - \vec{W} - \vec{T}_{(1,2)z} - \vec{T}_{(3,4)z}\right] - \Delta\vec{T}_{(1,2)z} = 0 - \Delta\vec{T}_{(1,2)z} = -\Delta\vec{T}_{(1,2)z} \quad \text{(A2)}$$

Note that the first set of terms can be eliminated due to the design of the hover conditions. The overall result, however, yields an unwanted, net negative (sink-inducing) thrust. Intuitively, we may reason that we can overcome this with a *balanced thrust* increase approach, which is described in Case 2 of the main text. Examining the sum of the moments about G gives Equation (A3):

$$\begin{aligned}\sum M_G: \left[\left(T_{(1,2)x} - T_{(3,4)x}\right)d_{(C\to G)z}\right] + \Delta T_{(1,2)x}d_{(C\to G)z} &= [0] + \Delta T_{(1,2)x}d_{(C\to G)z} \\ &= \Delta T_{(1,2)x}d_{(C\to G)z}\end{aligned} \quad \text{(A3)}$$

An undesirable clockwise pitching moment is induced about the y axis at G. The magnitude of the unwanted moment is proportional to the increase in the horizontal thrust as well as the magnitude of distance between C and G.

Two challenges have thus arisen with this thrust protocol; increased thrust intended for level translation will result in an undesirable unbalanced vertical thrust as well as a pitching moment. The first issue is alleviated in Case 2, and the latter in Case 3. Although the Case 1 protocol does carry the advantages of a righting moment and a reduced pitching moment ($2\Delta\vec{L}_y$, compared with $4\Delta\vec{L}_y$) during translation caused by the increase in angular momentum (see Section 2.2.3), the unbalanced vertical thrust makes it a less desirable translation approach than Case 2.

Appendix A.2. Case 3: Co-Located C and G with Balanced Thrust Increase

Referring to Figure A2, we will first examine the forces in a hover for the Case 3 translation protocol (Equations (A4)–(A6)):

$$\sum F_X = 0 \to \vec{T}_{(1,2)x} = \vec{T}_{(3,4)x} \quad \text{(A4)}$$

$$\sum F_Z = 0 \to \vec{B} - \vec{W} - \vec{T}_{(1,2)z} - \vec{T}_{(3,4)z} = 0 \quad \text{(A5)}$$

$$\sum M_G = 0 \to \left(T_{(1,2)x} - T_{(3,4)x}\right)d_{(C\to G)z} = (0)(0) = 0 \quad \text{(A6)}$$

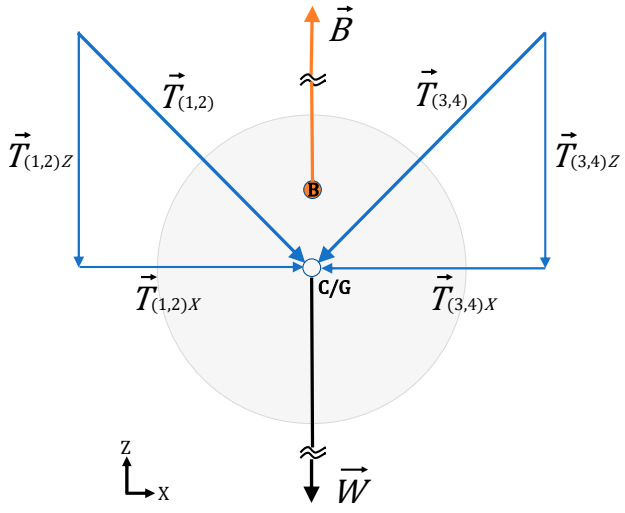

Figure A2. Case 3: Co-located C and G (hover state).

Next, we command a *balanced thrust* increase to induce $+x$ translation and examine the forces, as depicted in Figure A3.

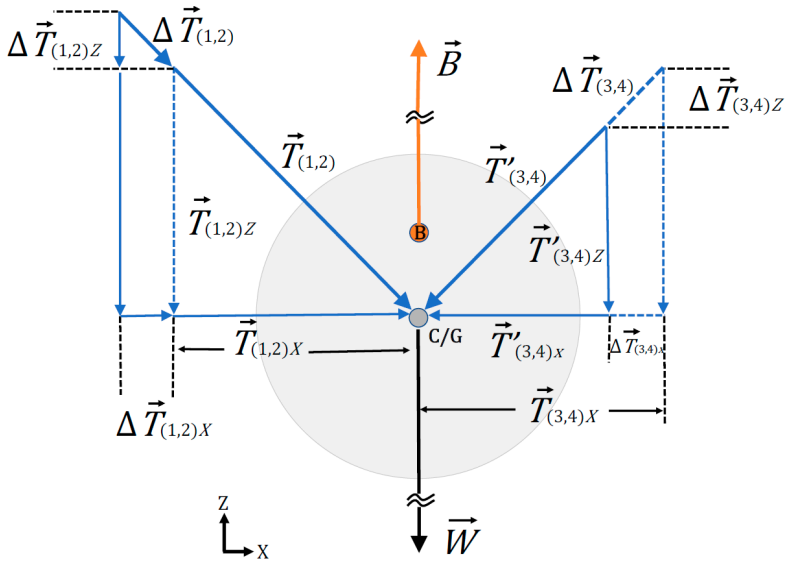

Figure A3. Case 3: Co-located C and G (with *balanced thrust* increase).

The corresponding static equations become ((A7)–(A9)):

$$\begin{aligned}\sum F_X: \; & \vec{T}_{(1,2)x} + \Delta\vec{T}_{(1,2)x} - \vec{T}\prime_{(3,4)x} \\ &= \vec{T}_{(1,2)x} + \Delta\vec{T}_{(1,2)x} - \left[\vec{T}_{(3,4)x} - \Delta\vec{T}_{(3,4)x}\right] \\ &= \left[\vec{T}_{(1,2)x} - \vec{T}_{(3,4)x}\right] + \Delta\vec{T}_{(1,2)x} + \Delta\vec{T}_{(3,4)x} \\ &= [0] + 2\Delta\vec{T}_x = 2\Delta\vec{T}_x\end{aligned} \tag{A7}$$

$$\begin{aligned}\sum F_Z: \; & \vec{B} - \vec{W} - \vec{T}_{(1,2)z} - \vec{T}\prime_{(3,4)z} - \Delta\vec{T}_{(1,2)z} \\ &= \vec{B} - \vec{W} - \vec{T}_{(1,2)z} - \left[\vec{T}_{(3,4)z} - \Delta\vec{T}_{(3,4)z}\right] - \Delta\vec{T}_{(1,2)z} \\ &= \left[\vec{B} - \vec{W} - \vec{T}_{(1,2)z} - \vec{T}_{(3,4)z}\right] + \Delta\vec{T}_{(3,4)z} - \Delta\vec{T}_{(1,2)z} \\ &= [0] + \Delta\vec{T}_z - \Delta\vec{T}_z = 0\end{aligned} \tag{A8}$$

$$\sum M_G = 0 \tag{A9}$$

Case 3 retains the benefits of the *balanced thrust* increase realized in Case 2 (vertical equilibrium) with the added benefit of having no unwanted translation-induced moment, since all the forces act through the center-of-gravity. The chief disadvantage of Case 3, apart from the technical difficulty of component ballasting to achieve perfect C and G co-location, is the significant reduction of the righting moment, which would entirely depend on separation of C and B. Without a righting moment, the yaw-induced moment would be unopposed.

References

1. Eldred, R.A. Autonomous Underwater Vehicle Architecture Synthesis for Shipwreck Interior Exploration. Master's Thesis, Naval Postgraduate School, Monterey, CA, USA, 2015.
2. Allotta, B.; Costanzi, R.; Ridolfi, A.; Salvetti, O.; Reggiannini, M.; Kruusmaa, M.; Salumae, T.; Lane, D.M.; Frost, G.; Tsiogkas, N.; et al. The ARROWS Project: Robotic technologies for underwater archaeology. In *IOP Conference Series: Materials Science and Engineering*; IOP Publishing: Bristol, UK, 2018; Volume 364.

3. Watson, S.; Daniel, A.D.; Keir, G. Localisation of Unmanned Underwater Vehicles (UUVs) in Complex and Confined Environments: A Review. *Sensors* **2020**, *21*, 6203. [CrossRef] [PubMed]
4. Bennett, M.T. Détente in deep water: The CIA mission to salvage a sunken Soviet submarine and US-USSR relations, 1968–1975. *Intell. Natl. Secur.* **2018**, *33*, 196–210. [CrossRef]
5. Kurson, R. *Shadow Divers.: The True Adventure of Two Americans Who Risked Everything to Solve One of the Last Mysteries of World War II*; Random House: New York, NY, USA, 2004.
6. Grządziel, A. Using Remote Sensing Data to Identify Large Bottom Objects: The Case of World War II Shipwreck of General von Steuben. *Geosciences* **2020**, *10*, 240. [CrossRef]
7. Radio Free Europe/Radio Liberty, Inc. Komsomolets Wreck Site Reveals High Radiation Levels 30 Years After Soviet Sub Sinks. 2021. Available online: https://www.rferl.org/a/komsomolets-wreck-site-reveals-high-radiation-levels-30-years-after-soviet-sub-sinks/30049952.html/ (accessed on 9 February 2021).
8. Høibråten, S.; Thoresen, P.E.; Are, H. The sunken nuclear submarine Komsomolets and its effects on the environment. *Sci. Total Environ.* **1997**, *202*, 67–78. [CrossRef]
9. Sellers, W. A Titanic Tale: A Former Alvin Pilot Recalls His 1986 Dives on the Shipwreck. 2010. Available online: https://www.whoi.edu/oceanus/feature/a-titanic-tale (accessed on 12 February 2021).
10. Ødegård, Ø.; Sorensen, A.J.; Hansen, R.E.; Ludvigsen, M. A new method for underwater archaeological surveying using sensors and unmanned platforms. *IFAC-PapersOnLine* **2016**, *49*, 486–493. [CrossRef]
11. Ward, C.; Ballard, R.D. Deep-water archaeological survey in the Black Sea: 2000 season. *Int. J. Naut. Archaeol.* **2004**, *33*, 2–13. [CrossRef]
12. Ballard, R.D. Archaeological oceanography. In *Remote Sensing in Archaeology*; Springer: New York, NY, USA, 2006; pp. 479–497.
13. Foley, B.P.; Dellaporta, K.; Sakellariou, D.; Bingham, B.S.; Camilli, R.; Eustice, R.M.; Evagelistis, D.; Ferrini, V.L.; Katsaros, K.; Kourkoumelis, D.; et al. The 2005 Chios Ancient Shipwreck Survey: New Methods for Underwater Archaeology. In *Hesperia: The Journal of the American School of Classical Studies at Athens*; 2009; Volume 78, pp. 269–305, JSTOR; Available online: www.jstor.org/stable/25622694 (accessed on 16 February 2021).
14. Allotta, B.; Brandani, L.; Casagli, N.; Costanzi, R.; Mugnai, F.; Monni, N.; Natalini, M.; Ridolfi, A. Development of Nemo remotely operated underwater vehicle for the inspection of the Costa Concordia wreck. In Proceedings of the Institution of Mechanical Engineers, Part M. *J. Eng. Marit. Environ.* **2017**, *231*, 3–18.
15. Rutledge, J.; Yuan, W.; Wu, J.; Freed, S.; Lewis, A.; Wood, Z.; Gambin, T.; Clark, C. Intelligent shipwreck search using autonomous underwater vehicles. In Proceedings of the 2018 IEEE International Conference on Robotics and Automation (ICRA), Brisbane, QLD, Australia, 21–25 May 2018.
16. L3Harris. IVER3 Autonomous Underwater Vehicle (AUV) spec sheet. 2019. Available online: https://www.l3harris.com/sites/default/files/2020-07/ims_maritime_datasheet_oceanserver_Iver3-Standard-Spec-Sheet.pdf/ (accessed on 17 February 2021).
17. Kapetanović, N.; Kordić, B.; Vasilijević, A.; Nađ, Đ.; Mišković, N. Autonomous Vehicles Mapping Plitvice Lakes National Park, Croatia. *Remote Sens.* **2020**, *12*, 3683. [CrossRef]
18. Kapetanović, N.; Vasilijević, A.; Nađ, Đ.; Zubčić, K.; Mišković, N. Marine Robots Mapping the Present and the Past: Unraveling the Secrets of the Deep. *Remote Sens.* **2020**, *12*, 3902. [CrossRef]
19. Mogstad, A.A.; Ødegård, Ø.; Nornes, S.M.; Ludvigsen, M.; Johnsen, G.; Sørensen, A.J.; Berge, J. Mapping the Historical Shipwreck Figaro in the High Arctic Using Underwater Sensor-Carrying Robots. *Remote Sens.* **2020**, *12*, 997. [CrossRef]
20. Rust, I.C.; Asada, H.H. The Eyeball ROV: Design and Control of a Spherical Underwater Vehicle Steered by an Internal Eccentric Mass. In Proceedings of the IEEE International Conference on Robotics and Automation, Shanghai, China, 9–13 May 2011; pp. 5855–5862.
21. Gongwer, C.A. Spherical Underwater Vehicle. U.S. Patent No. 4,455,962, 26 June 1984.
22. Xiao-juan, L.A.N.; Qing-xuan, J.I.A.; Han-xu, S.U.N. Principle and Dynamic Analysis of a New Type Spherical Underwater Vehicle. *J. Beijing Univ. Posts Telecommun.* **2010**, *33*, 20.
23. Kim, J.; Taesik, K.; Son-Cheol, Y. Conceptual Design of a Spherical Underwater Vehicle Equipped with Vertically Rotatable Thruster Units. In Proceedings of the 2018 IEEE/OES Autonomous Underwater Vehicle Workshop (AUV), Porto, Portugal, 6–9 November 2018.
24. Watson, S.A.; Peter, N.G. Depth control for micro-autonomous underwater vehicles (μAUVs): Simulation and experimentation. *Int. J. Adv. Robot. Syst.* **2014**, *11*, 31. [CrossRef]
25. Watson, S.A.; Dominic, J.P.C.; Peter, N.G. The design and technical challenges of a micro-autonomous underwater vehicle (μAUV). In Proceedings of the 2011 IEEE International Conference on Mechatronics and Automation, Beijing, China, 7–10 August 2011.
26. Mazumdar, M.S.T.; Asada, H.H. Dynamic Analysis and Design of Spheroidal Underwater Robots for Precision Multidirectional Maneuvering. In Proceedings of the IEEE/ASME Transactions on Mechatronics. *IEEE* **2015**, *20*, 2890–2902. [CrossRef]
27. Mazumdar, A.; Chuah, M.Y.; Triantafyllou, M.S.; Asada, H.H. Design for precision multi-directional maneuverability: Egg-shaped underwater robots for infrastructure inspection. In Proceedings of the 2014 IEEE International Conference on Robotics and Automation (ICRA), Hong Kong, China, 31 May–7 June 2014.
28. Mazumdar, A.; Asada, H.H. Control-configured design of spheroidal, appendage-free, underwater vehicles. *IEEE Trans. Robot.* **2013**, *30*, 448–460. [CrossRef]

29. Mazumdar, A.; Fittery, A.; Ubellacker, W.; Asada, H.H. A ball-shaped underwater robot for direct inspection of nuclear reactors and other water-filled infrastructure. In Proceedings of the 2013 IEEE International Conference on Robotics and Automation, Karlsruhe, Germany, 6–10 May 2013.
30. Fittery, A.; Mazumdar, A.; Lozano, M.; Asada, H.H. Omni-Egg: A smooth, spheroidal, appendage free underwater robot capable of 5 dof motions. In Proceedings of the 2012 Oceans, Hampton Roads, VA, USA, 14–19 October 2012.
31. Mazumdar, A.; Lozano, M.; Fittery, A.; Asada, H.H. A compact, maneuverable, underwater robot for direct inspection of nuclear power piping systems. In Proceedings of the 2012 IEEE International Conference on Robotics and Automation, Saint Paul, MN, USA, 14–18 May 2012.
32. Xing, H.; Guo, S.; Shi, L.; Hou, X.; Liu, Y.; Liu, H.; Hu, Y.; Xia, D.; Li, Z. A Novel Small-scale Turtle-inspired Amphibious Spherical Robot. In Proceedings of the IEEE/RSJ International Conference on Intelligent Robots and Systems (IROS), Macau, China, 4–8 November 2019.
33. Gary, M.O.; Fairfield, N.; Stone, W.C.; Wettergreen, D.; Kantor, G.; Sharp, J.M., Jr. 3D mapping and characterization of Sistema Zacato´n from DEPTHX (DEep Phreatic THermal eXplorer). In Proceedings of the 11th Multidisciplinary Conference on Sinkholes and Engineering and Environmental Impacts of Karst, Tallahassee, FL, USA, 22–26 September 2008; Yuhr, L.B., Alexander, E.C., Jr., Beck, B.F., Eds.; Geotechnical Special Publication no. 183. American Society of Civil Engineers: Reston, VA, USA, 2008; pp. 202–212. [CrossRef]
34. Richmond, K.; Gulati, S.; Flesher, C.; Hogan, B.P.; Stone, W.C. Navigation, control, and recovery of the ENDURANCE under-ice hovering AUV. In Proceedings of the International Symposium on Unmanned, Untethered Submersible Technology (UUST), Durham, NH, USA, 23–26 August 2009; AUSI: Lee, NH, USA, 2009.
35. Soylu, S.; Hampton, P.; Crees, T.; Woodroffe, A.; Jackson, E. Sonar-Based SLAM Navigation in Flooded Confined Spaces with the IMOTUS-1 Hovering AUV. Sonar-Based SLAM Navigation in Flooded Confined Spaces with the IMOTUS-1 Hovering AUV. In Proceedings of the 2018 IEEE/OES Autonomous Underwater Vehicle Workshop (AUV), Porto, Portugal, 6–9 November 2018.
36. Choi, H.-T.; Hanai, A.; Choi, S.K.; Yuh, J. Development of an underwater robot, ODIN-III. In Proceedings of the 2003 IEEE/RSJ International Conference on Intelligent Robots and Systems (IROS 2003) Cat. No. 03CH37453, Las Vegas, NV, USA, 27–31 October 2003.
37. Antonelli, G.; Chiaverini, S.; Sarkar, N.; West, M. Adaptive control of an autonomous underwater vehicle: Experimental results on ODIN. *IEEE Trans. Control. Syst. Technol.* **2001**, *9*, 756–765. [CrossRef]
38. Yang, K.C.H.; Junku, Y.; Song, K.C. Fault-tolerant system design of an autonomous underwater vehicle ODIN: An experimental study. *Int. J. Syst. Sci.* **1999**, *30*, 1011–1019. [CrossRef]
39. Choi, S.K.; Takashige, G.Y.; Yuh, J. Experimental study on an underwater robotic vehicle: ODIN. In Proceedings of the IEEE Symposium on Autonomous Underwater Vehicle Technology (AUV'94), Cambridge, MA, USA, 19–20 July 1994; pp. 79–84. [CrossRef]
40. Gu, S.; Shuxiang, G. Performance evaluation of a novel propulsion system for the spherical underwater robot (SURIII). *Appl. Sci.* **2017**, *7*, 1196. [CrossRef]
41. Li, Y.; Shuxiang, G.; Yu, W. Design and characteristics evaluation of a novel spherical underwater robot. *Robot. Auton. Syst.* **2017**, *94*, 61–74. [CrossRef]
42. Li, Y.; Shuxiang, G.; Chunfeng, Y. Study on the control system of a novel spherical underwater robot. In Proceedings of the 2015 IEEE International Conference on Mechatronics and Automation (ICMA, Beijing, China, 2–5 August 2015.
43. Li, Y.; Shuxiang, G.; Chunfeng, Y. Preliminary concept of a novel spherical underwater robot. *Int. J. Mechatron. Autom.* **2015**, *5*, 11–21. [CrossRef]
44. Yue, C.; Guo, S.; Li, M.; Li, Y. Passive and active attitude stabilization method for the spherical underwater robot (SUR-II). In Proceedings of the 2013 IEEE International Conference on Robotics and Biomimetics (ROBIO), Shenzhen, China, 12–14 December 2013.
45. Yue, C.; Guo, S.; Li, M.; Shi, L. Electrical system design of a spherical underwater robot (SUR-II). In Proceedings of the 2013 IEEE International Conference on Information and Automation (ICIA), Yinchuan, China, 2–28 August 2013.
46. Yue, C.; Shuxiang, G.; Maoxun, L. ANSYS FLUENT-based modeling and hydrodynamic analysis for a spherical underwater robot. In Proceedings of the 2013 IEEE International Conference on Mechatronics and Automation, Takamatsu, Japan, 4–7 August 2013.
47. Yue, C.; Shuxiang, G.; Liwei, S. Hydrodynamic analysis of the spherical underwater robot SUR-II. *Int. J. Adv. Robot. Syst.* **2013**, *10*, 247. [CrossRef]
48. Lin, X.; Shuxiang, G. Development of a spherical underwater robot equipped with multiple vectored water-jet-based thrusters. *J. Intell. Robot. Syst.* **2012**, *67*, 307–321. [CrossRef]
49. Yue, C.; Guo, S.; Lin, X.; Du, J. Analysis and improvement of the water-jet propulsion system of a spherical underwater robot. In Proceedings of the 2012 IEEE International Conference on Mechatronics and Automation, Chengdu, China, 5–8 August 2012.
50. Lin, X.; Guo, S.; Tanaka, K.; Hata, S. Underwater experiments of a water-jet-based spherical underwater robot. In Proceedings of the 2011 IEEE International Conference on Mechatronics and Automation, Beijing, China, 7–10 August 2011.
51. Guo, S.; Du, J.; Ye, X.; Yan, R.; Gao, H. The computational design of a water jet propulsion spherical underwater vehicle. In Proceedings of the 2011 IEEE International Conference on Mechatronics and Automation, Beijing, China, 7–9 August 2011.
52. Guo, S.; Lin, X.; Tanaka, K.; Hata, S. Development and control of a vectored water-jet-based spherical underwater vehicle. In Proceedings of the 2010 IEEE International Conference on Information and Automation, Harbin, China, 20–23 June 2010.

53. Robador, E.M.; Hansen, G.M.; Acha, L.; Pedre, S. Design of an AUV for visual inspection of nuclear power plants. In Proceedings of the 2018 IEEE/OES Autonomous Underwater Vehicle Workshop (AUV), Porto, Portugal, 6–9 November 2018.
54. Milosevic, Z.; Fernandez, R.A.S.; Dominguez, S.; Rossi, C. Guidance for Autonomous Underwater Vehicles in Confined Semistructured Environments. *Sensors* **2020**, *20*, 7237. [CrossRef]
55. Fernandez, R.A.S.; Milovsevic, Z.; Dominguez, S.; Rossi, C. Motion Control of Underwater Mine Explorer Robot UX-1: Field Trials. *IEEE Access* **2019**, *7*, 99782–99803. [CrossRef]
56. Fernandez, R.A.S.; Milovsevic, Z.; Dominguez, S.; Rossi, C. Modeling and control of underwater mine explorer robot UX-1. *IEEE Access* **2019**, *7*, 39432–39447. [CrossRef]
57. Fernandez, R.A.S.; Milovsevic, Z.; Dominguez, S.; Rossi, C. Nonlinear attitude control of a spherical underwater vehicle. *Sensors* **2019**, *19*, 1445. [CrossRef] [PubMed]
58. Fernandez, R.A.S.; Milosevic, Z.; Dominguez, S.; Rossi, C. Design, Modeling and Control of a Spherical Autonomous Underwater Vehicle for Mine Exploration. In Proceedings of the 2018 IEEE/RSJ International Conference on Intelligent Robots and Systems (IROS), Madrid, Spain, 1–5 October 2018; pp. 1513–1519. [CrossRef]
59. Martins, A.; Almeida, J.; Almeida, C.; Dias, A.; Dias, N.; Aaltonen, J.; Heininen, A.; Koskinen, K.T.; Rossi, C.; Dominguez, S.; et al. UX 1 system design-A robotic system for underwater mining exploration. In Proceedings of the 2018 IEEE/RSJ International Conference on Intelligent Robots and Systems (IROS), Madrid, Spain, 1–5 October 2018.
60. Zavari, S.; Heininen, A.; Aaltonen, J.; Koskinen, K.T. Early stage design of a spherical underwater robotic vehicle. In Proceedings of the 2016 20th International Conference on System Theory, Control and Computing (ICSTCC), Sinaia, Romania, 13–15 October 2016.
61. Raspberry Pi Foundation. Raspberry Pi 4 Tech Specs. 2021. Available online: https://www.raspberrypi.org/products/raspberry-pi-4-model-b/specifications/ (accessed on 7 February 2021).
62. Blue Robotics. T100 Thruster (Retired) Product Description. 2021. Available online: https://bluerobotics.com/store/retired/t100-thruster/ (accessed on 7 February 2021).
63. Herman, P. Numerical Test of Several Controllers for Underactuated Underwater Vehicles. *Appl. Sci.* **2020**, *10*, 8292. [CrossRef]
64. Sands, T. Development of Deterministic Artificial Intelligence for Unmanned Underwater Vehicles (UUV). *J. Mar. Sci. Eng.* **2020**, *8*, 578. [CrossRef]
65. Álvarez-Tuñón, O.; Rodriguez, A.; Jardon, A.; Balaguer, C. Underwater Robot Navigation for Maintenance and Inspection of Flooded Mine Shafts. In Proceedings of the 2018 IEEE/RSJ International Conference on Intelligent Robots and Systems (IROS), Madrid, Spain, 1–5 October 2018.
66. Chaudhary, M.; Conrad, M.J. A Survey on the Implementation of Wireless Sensor Network Breadcrumb Trails for Sensing and Localization. In Proceedings of the 2019 SoutheastCon, Huntsville, AL, USA, 11–14 April 2019.
67. Sumantr, B.; Karsiti, M.N.; Agustiawan, H. Development of variable ballast mechanism for depth positioning of spherical URV. In Proceedings of the 2008 International Symposium on Information Technology, Kuala Lumpur, Malaysia, 26–28 August 2008.